



<p><b>HORIZON 2020</b></p>   <p>Terahertz based Ultra High Bandwidth Wireless Access Networks</p>		Deliverable ID:	Preparation date:
		D4.4	06 May 2020
		Milestone: released	
		Title:	
		<p><b>Final Characterisation of Systems</b></p>	
		<p>Editor/Lead beneficiary (name/partner):</p> <p>Johannes Eckhardt / TUBS</p>	
		<p>Internally reviewed by (name/partner):</p> <p>Mira Naftaly / NPL</p> <p>Marco Garcia Porcel / VLC</p>	
		<p>Approved by:</p> <p>PSC</p>	
<p><b>Dissemination level</b></p>			
<b>PU</b>	Public	x	
<b>CO</b>	Confidential, only for members of the consortium (including Commission Services)		

Revisions				
Version	Date	Author	Organisation	Details
1.0	04.12.19	Johannes Eckhardt	TUBS	structure and first chapters added
2.0	02.03.20	Johannes Eckhardt	TUBS	major contributions added
3.0	06.04.20	Johannes Eckhardt	TUBS	final version
4.0	30.04.20	Johannes Eckhardt	TUBS	review comments integrated

The research leading to these results has received funding from the EU H2020 under grant agreement n° 761579.



## Table of contents

Table of contents .....	iii
List of figures .....	v
List of tables .....	vi
Executive summary .....	1
1 Introduction .....	3
1.1 Motivation.....	3
1.2 Structure of this document .....	3
1.3 Relationships with other deliverables .....	3
1.4 Contributors .....	3
1.5 Acronyms and abbreviations.....	3
2 Channel Measurements .....	5
2.1 Measurement Campaign .....	5
2.2 Measurement Calibration.....	6
2.2.1 Theoretical Principles of Deconvolution .....	6
2.2.2 Deconvolution with a fixed window.....	8
2.2.3 Deconvolution with an adaptive window .....	9
2.2.4 Processing of the measured data with simplified calibration .....	11
2.3 Measurement Evaluation GUI .....	12
2.4 Inter-rack Measurements .....	15
2.5 Intra-rack Measurements .....	25
3 Channel Simulations.....	30
3.1 Ray-Tracing Simulations .....	30
3.2 3D Model Building .....	31
3.3 Material Parameter Calibration.....	33
3.3.1 Categorization of Materials in Datacentre .....	35
3.3.2 Comparison of Measurement and Simulation .....	37
3.4 Stochastic Channel Modelling .....	44
3.4.1 Propagation path types.....	45
3.4.2 Statistical Delay Distribution.....	46
3.4.3 Delay-Path loss Correlation.....	47
3.4.4 Angle of Departure (AoD) and Angle of Arrival (AoA) .....	48
3.4.5 Angle-Path loss Correlation.....	49
4 Transmission Measurements in the Environmental Chamber .....	51
5 Conclusion/Further work.....	55
References .....	56





## List of figures

Figure 1: Dell EMC Research Data Centre .....	5
Figure 2: Schematic view of the channel sounder .....	6
Figure 3: LTI system .....	6
Figure 4: Window function .....	8
Figure 5: Result before and after deconvolution; same data used for measurement and B2B .....	8
Figure 6: Result before and after deconvolution; two different B2B measurements used as input data .....	9
Figure 7: Result before and after deconvolution; two different B2B measurements (UWB) used as input data .....	9
Figure 8: Amplitude spectrum of measurement and corresponding Wiener window function .....	11
Figure 9: Result before and after deconvolution; two different B2B measurements .....	11
Figure 10: Exemplary measurement with noise floor and threshold levels .....	12
Figure 11: Result after calibration .....	12
Figure 12: Post-processing graphic user interface (GUI) .....	13
Figure 13: Omnidirectional channel impulse response of GC lcv .....	16
Figure 14: ODCIR of GC FO scv .....	16
Figure 15: ODCIR of GC FO sch .....	17
Figure 16: ODCIR of GC FO lhv .....	18
Figure 17: ODCIR of ToR sav .....	19
Figure 18: ODCIR of ToR aav .....	19
Figure 19: ODCIR of ToR aah .....	20
Figure 20: ODCIR of ToR ntaav .....	20
Figure 21: ODCIR of ToR ntaah .....	21
Figure 22: PAP of GC FO lcv .....	22
Figure 23: PAP of GC FO scv .....	22
Figure 24: PAP of GC FO sch .....	23
Figure 25: PAP of GC FO lhv .....	23
Figure 26: PAP of ToR FO sav .....	24
Figure 27: PAP of ToR FO aav .....	24
Figure 28: PAP of ToR FO aah .....	24
Figure 29: PAP of ToR FO ntaav .....	25
Figure 30: PAP of ToR FO ntaah .....	25
Figure 31: Measurement setup of the Intra-rack measurement; left: short distance, middle: medium distance, right: long distance .....	26
Figure 32: IR of the B2B measurement (blue) and the Intra-rack measurement No. 01 (orange) .....	27
Figure 33: Measurement setup No. 6 (left) and No. 17 (right) .....	28
Figure 34: IR of measurement No. 6 (blue) and No. 17 (orange) .....	29
Figure 35: Functional Block of SiMoNe .....	30
Figure 36: Dell EMC Unity All Flash Photo (left) and 3D Model (right) .....	31
Figure 37: Exemplary Building 3D Collection based on generic Importer .....	33
Figure 38: 3D Model of the Dell EMC Research Data Centre .....	33
Figure 39: Illustration of propagating electromagnetic wave trough a medium having different refractive index .....	34
Figure 40: Refractive index of the plastic curtains .....	36
Figure 41: Absorption coefficient of the plastic curtains .....	36
Figure 42: setup of GC FO lcv in the DC (left) and in SiMoNe (right) .....	37
Figure 43: Comparison of the GC measurement and ray tracing simulation .....	37
Figure 44: setup and ray tracing of ToR FO sa .....	38
Figure 45: Comparison of the ToR measurement and ray tracing simulation .....	38
Figure 46: Writing desk at the end of the aisle .....	40



Figure 47: Variation of reflection attenuation with different thickness of interaction material using transfer-matrix model .....	41
Figure 48: 3D (left) and 2D (right) depiction of reflection loss against thickness and real part of relative permittivity using transfer-matrix method.....	43
Figure 49: 3D (left) and 2D (right) depiction of reflection loss against angle of incidence and real part of relative permittivity using transfer-matrix method .....	43
Figure 50: 3D (left) and 2D (right) depiction of reflection loss against angle of incidence and thickness of interaction material using transfer-matrix method.....	44
Figure 51: Exemplary TX-RX position limiting interaction region within Chamber (Left); through Chamber (right) .....	45
Figure 52: Propagation path types.....	46
Figure 53: Delay distributions of each type of propagation paths.....	46
Figure 54: Delay-Path loss correlation distribution.....	47
Figure 55: Probability of Angle of Departure (left) and Angle of Arrival (right) of type 1: direct.....	48
Figure 56: Probability of Angle of Departure (left) and Angle of Arrival (right) of type 2: 1 <sup>st</sup> reflected .....	48
Figure 57: Probability of Angle of Departure (left) and Angle of Arrival (right) of type 3: 2 <sup>nd</sup> reflected .....	49
Figure 58: Probability of Angle of Departure (left) and Angle of Arrival (right) of type 4: transmitted .....	49
Figure 59: Probability of Angle Path loss Correlation of type 1: direct.....	49
Figure 60: Probability of Angle Path loss Correlation of type 2: 1 <sup>st</sup> reflected .....	50
Figure 61: Probability of Angle Path loss Correlation of type 3: 2 <sup>nd</sup> reflected .....	50
Figure 62: Probability of Angle Path loss Correlation of type 4: transmitted.....	50
Figure 63: Photograph of the environmental chamber employed in transmission measurements .....	51
Figure 64: Schematic diagram of the THz beam path in the transmission measurement setup .....	51
Figure 65: Atmospheric attenuation due to absorption by gases. Dry: 2.2 g/m <sup>3</sup> H <sub>2</sub> O; standard: 7.5 g/m <sup>3</sup> H <sub>2</sub> O. From ITU-R P.676-12. ....	52
Figure 66: Dependence of water vapour content on ambient relative humidity and temperature.....	53
Figure 67: Expected atmospheric attenuation at 100, 220 and 300 GHz as a function of H <sub>2</sub> O density 53	
Figure 68: Transmission signal at 100, 220 and 300 GHz as a function of water vapour density, showing absence of detectable dependence. ....	54
Figure 69: Attenuation by water vapour at 557 GHz, showing agreement with literature.....	54

## List of tables

Table 1: Cut-off frequencies.....	8
Table 2: List if GC FO setups .....	15
Table 3: Striking MPCs of GC FO lcv and GC FO scv .....	16
Table 4: Polarisation dependent comparison of the path loss .....	17
Table 5: List of ToR FO setups .....	18
Table 6: Delay spread and angular spread of all FO measurements .....	21
Table 7: Intra-rack measurement setups.....	26
Table 8: Direct path characteristics of intra-rack measurements .....	27
Table 9: Generic Importer CSV-File Parameters .....	31
Table 10: Material parameters depending on material category .....	36
Table 11: Comparison of six different free space path loss .....	38
Table 12: Comparison of measured value and simulated value of reflection attenuation at materials .	39
Table 13: refractive coefficient and resulted angle between air and curtain (new).....	42
Table 14: reflection and transmission coefficient between air and curtain .....	42
Table 15: Number of existing rays depending on path types .....	46
Table 16: Values of parameters and type of delay distribution in terms path types.....	46









## Executive summary

This deliverable presents the main results of task T4.2 of work package 4 of the TERAPOD project. First, the measurement campaign and the methodology are explained. The corresponding analysis shows the different aspects of the spatial and temporal characteristics of the THz channel in a data centre environment.

Ray tracing simulations in the 3D model of the data centre are presented showing meaningful results that reflect the real propagation captured during the measurement campaign.

The stochastic channel modelling is performed providing a model for further use in more abstract and higher layer simulation tools.

Finally, the measurements in the environmental chamber at NPL confirm negligible attenuation by atmospheric absorption under the conditions in a data centre.





# 1 Introduction

## 1.1 Motivation

The aim of TERAPOD is to introduce wireless links in a data centre network. An important part in the design of a new communications system in the THz band constitutes the radio channel. The channel influences the development of the communication system directly. Therefore, a good and profound knowledge of the radio channel at THz frequencies in a data centre is mandatory. Task 2 in work package 4 is dedicated the investigation of the THz radio channel by measurement and simulation. An extensive three week measurement campaign was carried out and a comprehensive simulation environment was set up based on ray tracing to model the THz propagation in the data centre.

## 1.2 Structure of this document

The deliverable is structured in three main parts. The first part deals with the measurement campaign in Ireland presenting the methodology and an in-depth analysis of spatial and temporal aspects of the radio channel. The second section describes the ray-tracing and presents the simulations results. The stochastic modelling is also part of the second section. The third and last section discusses the measurements in the environmental chamber that were carried out in cooperation between NPL and TUBS.

## 1.3 Relationships with other deliverables

The content presented in this document relates on the following deliverables:

- D2.1 – Initial Requirements and Scenario Specification
- D2.2 – Revised Requirements and Scenario Specification
- D4.3 – Initial Characterisation of Systems

## 1.4 Contributors

The following partners have contributed to this deliverable:

- Johannes Eckhardt, TUBS
- Bo Kum Jung, TUBS
- Tobias Doeker, TUBS
- Mira Naftaly, NPL
- Thomas Kürner, TUBS

## 1.5 Acronyms and abbreviations

B2B – Back-to-Back measurement

DC – Data Centre

FO – Full-Omi 360° rotational measurement

FSPL – Free space path loss

GC – General Characterisation measurement

HBPW – Half power beam width

IR – Impulse response

ISI – intersymbol interference

LOS – line-of-sight

MPC – Multipath component

NLOS – non line-of-sight



P2P – Point-to-Point

PAS – Power Angular Spectrum

PDP – Power Delay Profile

PL – Path loss

RX – receiver

ToR – Top-of-Rack

TX – transmitter

TZC – Time Zero Calibration



## 2 Channel Measurements

Channel characterisation is of great importance for the development of new communication systems. TERAPOD aims at integrating wireless links into a data centre (DC) network. Therefore, channel measurement and modelling plays an important role in order to build and adapt the physical layer and higher layers accordingly.

### 2.1 Measurement Campaign

The measurement campaign of the TERAPOD project was a three-week campaign in the Dell EMC Research Data Centre, Cork, Ireland and the TSSG Research Data Centre, Waterford, Ireland. In D4.3 [1] the different measurement categories were already defined and explained, so that only the naming will be recalled here. Based on the requirements and the use cases from D2.1 [2] and D2.2 [3], measurement setups were developed that investigate general propagation effects on the one hand and emulate real application scenarios on the other hand. We call the setup scenarios general characterisation (GC) and top-of-rack (ToR), respectively. Another category represents the intra-rack links which were also defined in the use cases and hence were measured during the measurement campaign. Nevertheless, the ToR scenarios promise a higher benefit for the DC and are therefore prioritised in TERAPOD. [4]

The Dell EMC Research Data Centre where the main part of the measurements were performed has a typical structure of a DC. A certain number of racks are placed in rows within a certain distance. In each aisle all racks are faced either with their front sides or their rear sides so that a consistent flow of the cooling air is introduced. Plastic curtains on top of the racks divide the sections into cold aisles and hot aisles as depicted in Figure 1. The major part of the measurements was done in the cold aisle and the hot aisle that are labelled in Figure 1 because they have a regular structure with regard to the distances and the rack shapes.

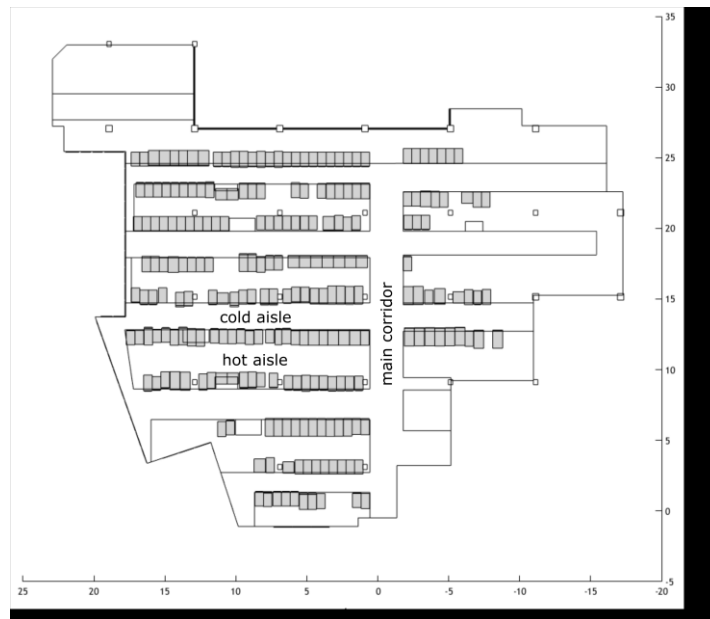


**Figure 1: Dell EMC Research Data Centre**

The measurements were performed with the UWB sub-THz channel sounder that was described in D4.3 [1]. Here, the basic functions of the channel sounder are repeated for a coherent understanding of the following results. Therefore, the schematic view of the channel sounder is explained which is presented in Figure 2. The base unit creates a common system clock of 9.22 GHz and distributes it via multi-function cables to the UWB modules. The transmitter (TX) UWB module creates the pseudo random test sequence (pseudo noise generator, PNG) with good autocorrelation properties that approximate the



Dirac delta function. This transmit signal is converted to the frequency range of interest by a frequency extender. Here, the resulting frequency band ranges from 300.2 GHz to 308.2 GHz.

The frequency extender at the receiver (RX) downconverts the signal back to the base band. The received signal is sampled by an analogue-to-digital converter with in-phase and quadrature using sub-sampling with a factor of 128. In the post-processing the cross correlation is calculated leading to the relative impulse response (IR) of the radio channel. [5]

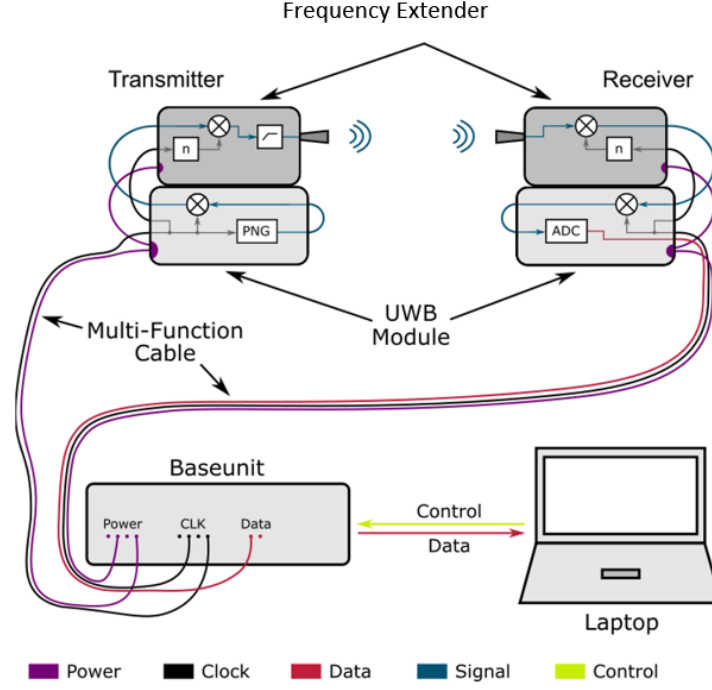


Figure 2: Schematic view of the channel sounder

## 2.2 Measurement Calibration

The basic objective of the calibration is to suppress artefacts in the Channel Impulse Response (CIR) which are caused by the system. The chosen approach is based on a deconvolution, where a Back-to-Back (B2B) measurement provides the basis. In the following the theoretical principles of the deconvolution are explained first. Hereinafter two slightly different variants of the deconvolution are introduced and compared before the finally used realization of the calibration and post processing is given.

### 2.2.1 Theoretical Principles of Deconvolution

Channel Sounding basically can be formulated by means of a linear time-invariant (LTI) system:

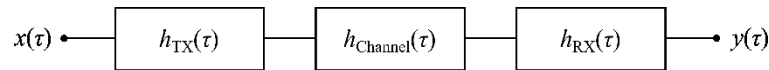


Figure 3: LTI system

In Figure 3  $x(t)$  and  $y(t)$  describe respectively the transmitted and received signal,  $h_{TX}(t)$  and  $h_{RX}(t)$  describe the impulse response of the transmitter (TX) and receiver (RX), and  $h_{Channel}(t)$  describes the impulse response of the measured channel. The received signal  $y(t)$  can be calculated as



$$y(t) = x(t) * h_{TX}(t) * h_{Channel}(t) * h_{RX}(t) \quad (2.1)$$

where  $*$  stands for the convolution. As the channel sounder measures the CIR, the CIR  $h_{Meas}(t)$  is given by

$$h_{Meas}(t) = \frac{y(t)}{x(t)} = h_{TX}(t) * h_{Channel}(t) * h_{RX}(t) \quad (2.2)$$

During a B2B measurement TX and RX are connected to each other directly. Therefore the measured signal can be calculated as

$$h_{B2B}(t) = h_{TX}(t) * h_{RX}(t) \quad (2.3)$$

Formula (2.2) than can be reformulated as

$$h_{Meas}(t) = h_{B2B}(t) * h_{Channel}(t) \quad (2.4)$$

In the frequency domain the measured CIR is then given by

$$H_{Meas}(f) = H_{B2B}(f) \cdot H_{Channel}(f) \quad (2.5)$$

where  $H_{Meas}(f)$ ,  $H_{B2B}(f)$  and  $H_{Channel}(f)$  describe the corresponding transfer functions in the frequency domain. The transfer function of the channel can be calculated as

$$H_{Channel}(f) = \frac{H_{Meas}(f)}{H_{B2B}(f)} \quad (2.6)$$

which is called deconvolution. Finally the inverse Fourier transform of formula (2.6) into the time domain gives the CIR.

The baseband bandwidth of the used channel sounder is 4.61 GHz. As the transmitted signal is band-limited by the use of an anti-alias filter, the bandwidth of the transmitted and received signal is approximately 4 GHz. Therefore in the frequency range from 4 GHz up to 4.61 GHz only noise is received. The received power in this frequency range is hence extremely low in contrast to the received power of the signal. When calculating the transfer function of the channel according to Formula (2.6) the extremely low values in the denominator results in very high multiplicative factors. To avoid this problem an additional window function is used to weigh the different sectors in the frequency domain. Thus, Formula (2.6) is reformulated as

$$H_{Channel}(f) = \frac{H_{Meas}(f)}{H_{B2B}(f)} \cdot H_{window}(f) \quad (2.7)$$

where  $H_{window}(f)$  describes the transfer function of the weight function. The window is similar to the transfer function of a bandpass filter: The window consists of a passband surrounded by stopbands. Here the transition emulates edges of known filter types. Figure 4 shows a schematic illustration of a window function.



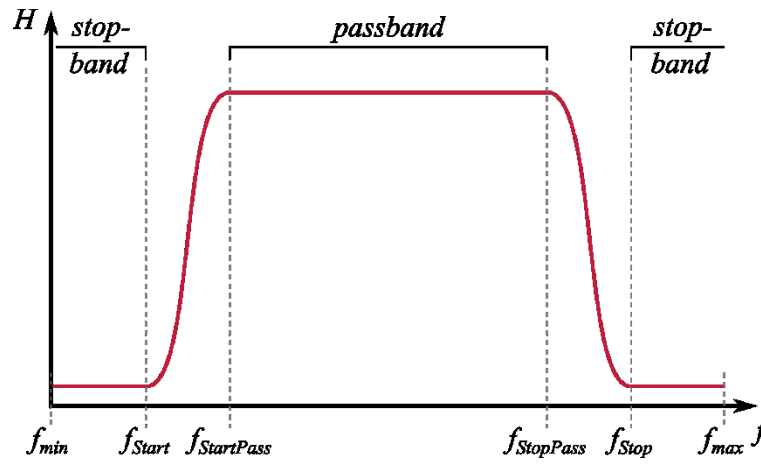


Figure 4: Window function

In the following two different approaches for the window will be presented and analyzed, whereby the first approach uses a fixed window and the second approach uses a window which is fitted in relation to the measured data.

### 2.2.2 Deconvolution with a fixed window

For the fixed window the transition between stopband and passband emulates the edges of a Hanning window. The cut-off frequencies are chosen as follows:

Table 1: Cut-off frequencies

$f_{\min}$	$f_{\text{Start}}$	$f_{\text{StartPass}}$	$f_{\text{StopPass}}$	$f_{\text{Stop}}$	$f_{\max}$
0.00 GHz	0.00 GHz	2.00 GHz	2.15 GHz	4.25 GHz	4.61 GHz

To verify the deconvolution with the fixed window according to Table 1 for the B2B measurement and the measurement which should be calibrated, the same data will be used. In this case the result should be the window function according to Formula (2.7) whereby  $H_{\text{Meas}}(f) = H_{\text{B2B}}(f)$ . Figure 5 shows the uncalibrated data in blue and the calibrated data in orange. It can be seen that the calibrated data equals the window function and therefore the deconvolution is verified.

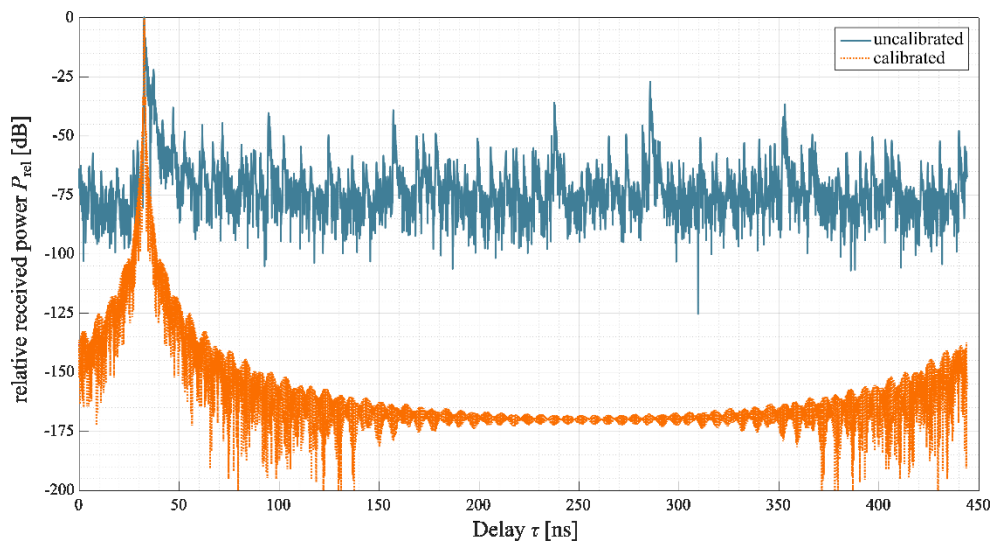
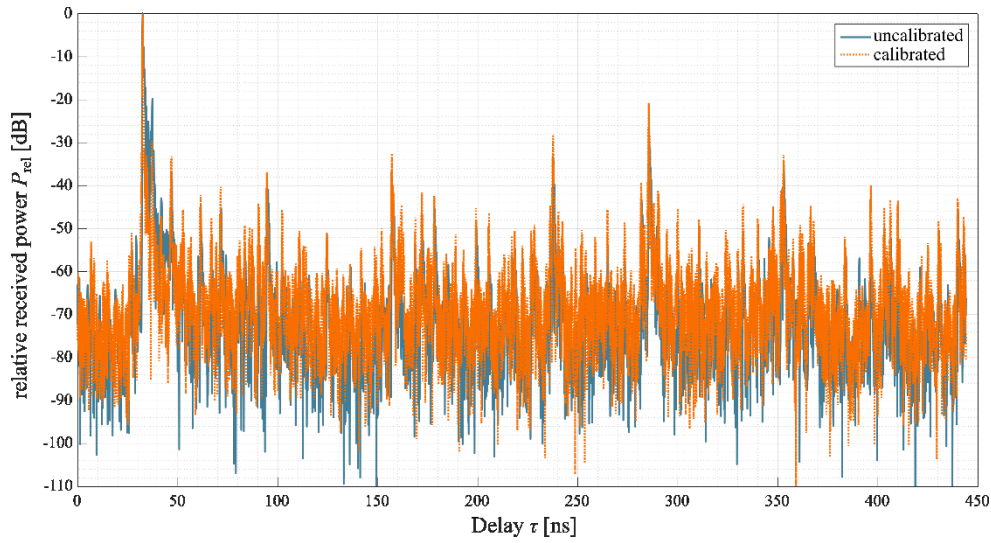


Figure 5: Result before and after deconvolution; same data used for measurement and B2B





In the next step data from two different B2B measurements will be used as the data for  $H_{B2B}(f)$  and  $H_{Meas}(f)$ , respectively. The uncalibrated and calibrated data is shown in Figure 6.



**Figure 6: Result before and after deconvolution; two different B2B measurements used as input data**

It can be seen, that the deconvolution does not produce usable results in this case. It was found that the signal of the channel sounder shows slight variations over time when using the frequency extenders. This instability leads to the dysfunction of the calibration algorithm. B2B measurements done in the baseband without the frequency extenders are stable over time and therefore the deconvolution produces good results, as shown in Figure 7.

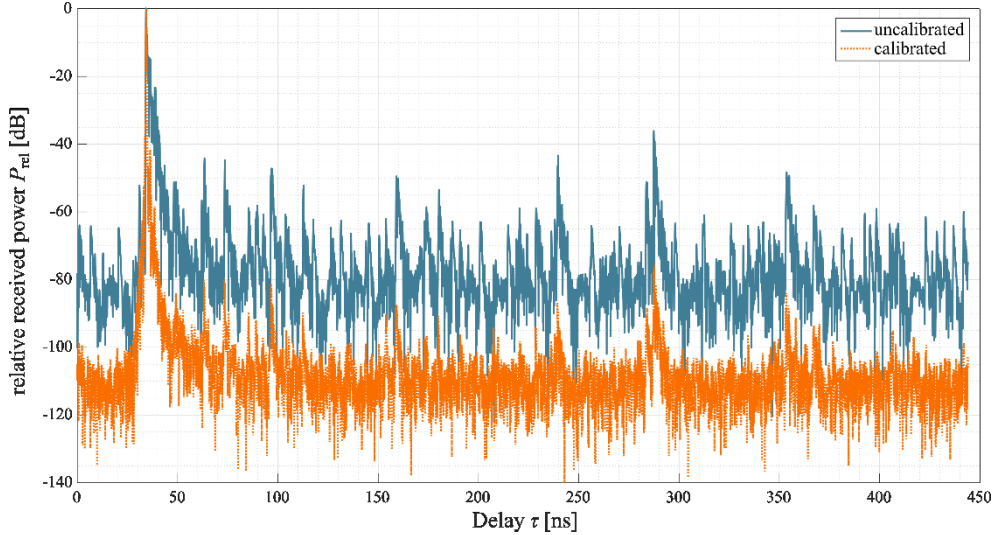


**Figure 7: Result before and after deconvolution; two different B2B measurements (UWB) used as input data**

In this case the deconvolution decreases the side pulses up to -40 dB so that the dynamic range increases up to approximately 70 dB. Nevertheless, under the given circumstances the deconvolution with a fixed window does not provide good results.

### 2.2.3 Deconvolution with an adaptive window

For this approach a Wiener window will be used which can be derived from a Wiener filter. The Wiener filter is a well-known filter in signal processing used to calculate an unknown signal. The measured



impulse response  $h_{\text{Meas}}(t)$  which should be calibrated, is assumed to be the result of a convolution of a known impulse response, here the B2B measurement  $h_{\text{B2B}}(t)$ , and the unknown impulse response of the channel sounder  $h_{\text{Channel}}(t)$ , plus noise  $n(t)$ :

$$h_{\text{Meas}}(t) = h_{\text{Channel}}(t) * h_{\text{B2B}}(t) + n(t) \quad . \quad (2.8)$$

Then, there is a filter  $w(t)$  which can estimate the CIR  $\hat{h}_{\text{Channel}}(t)$  by

$$\hat{h}_{\text{Channel}}(t) = h_{\text{Meas}}(t) * w(t) \quad \text{---} \bullet \quad \hat{H}_{\text{Channel}}(f) = H_{\text{Meas}}(f) \cdot W(f) \quad . \quad (2.9)$$

According to [6] the transfer function of the window is given by

$$W(f) = \frac{H_{\text{B2B}}^*(f) \cdot |H_{\text{Channel}}(f)|^2}{|H_{\text{B2B}}(f)|^2 \cdot |H_{\text{Channel}}(f)|^2 + |N(f)|^2} \quad (2.10)$$

whereby  $(\cdot)^*$  stands for a complex conjugate. By defining the signal-to-noise ratio (SNR) of the unknown signal in the frequency domain by

$$\text{SNR}(f) = \frac{|H_{\text{Channel}}(f)|^2}{|N(f)|^2} \quad (2.11)$$

Formula (2.10) can be reformulated as

$$W(f) = \frac{1}{H_{\text{B2B}}(f)} \cdot \left[ \frac{|H_{\text{B2B}}(f)|^2}{|H_{\text{B2B}}(f)|^2 + \frac{1}{\text{SNR}(f)}} \right] \quad . \quad (2.12)$$

The transfer function of the unknown signal then can be calculated by

$$\hat{H}_{\text{Channel}}(f) = H_{\text{Meas}}(f) \cdot W(f) = \frac{H_{\text{Meas}}(f)}{H_{\text{B2B}}(f)} \cdot \left[ \frac{|H_{\text{B2B}}(f)|^2}{|H_{\text{B2B}}(f)|^2 + \frac{1}{\text{SNR}(f)}} \right] \quad . \quad (2.13)$$

The first part of Formula (2.13) corresponds to the deconvolution according to Formula (2.6) and the part in square brackets corresponds to the Wiener window. It can be seen that the Wiener window is based on the SNR of the unknown signal, so that the SNR has to be estimated. The SNR estimation is quite costly, hence the procedure will not be described in detail at this point. However, it should be pointed out that the estimation is based on a Monte Carlo process as described in [7]. Figure 8 shows an exemplary window function calculated by the measured data.



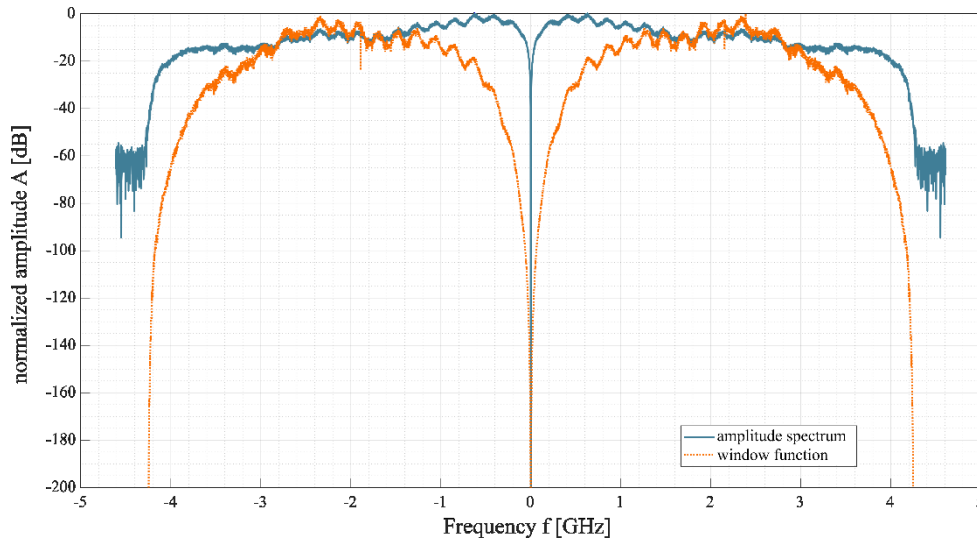


**Figure 8: Amplitude spectrum of measurement and corresponding Wiener window function**

Ultimately, tests of this approach have shown disappointing results. The unwanted side peaks could not be suppressed by the deconvolution. Furthermore, after the deconvolution additional side peaks arose in the CIR. Figure 9 shows a CIR before and after deconvolution. At approximately 240 ns an additional side peak can be seen.

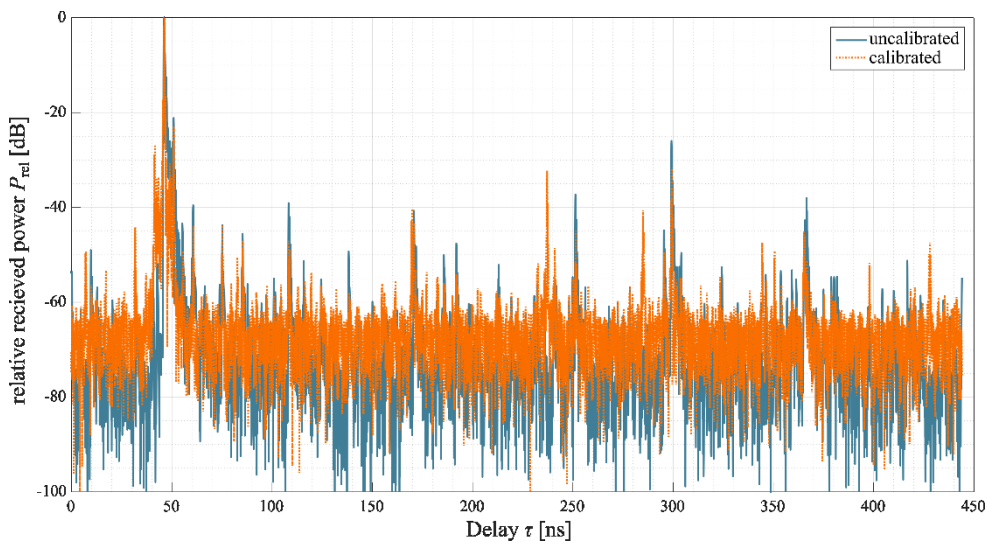


**Figure 9: Result before and after deconvolution; two different B2B measurements**

#### 2.2.4 Processing of the measured data with simplified calibration

The previous findings have shown that a calibration using a deconvolution does not lead to the desired results. Therefore a processing of the measured data without a calibration is presented below. It should be noted that this method also can be used additionally to a preceding calibration.

First of all the noise floor of the measured data is estimated. After that, all values below the noise floor plus a given threshold (typically 15 dB) will be set to zero, because in this case one cannot differentiate between noise and signal. The difference between the main pulse and the biggest spurious pulse, which is caused by the channel sounder system, can be seen from the B2B measurement as a reference. The measured values below the highest measured peak minus the spurious free dynamic range from the B2B measurement are also set to zero, because in this case one cannot clearly differentiate between multipath components and pulses caused by the system.



Furthermore with the B2B measurement the time offset of the measurement can be determined. Finally, synthetic generated noise is added. Figure 10 shows an exemplary measurement and the above mentioned thresholds and Figure 11 shows the result after the described method.

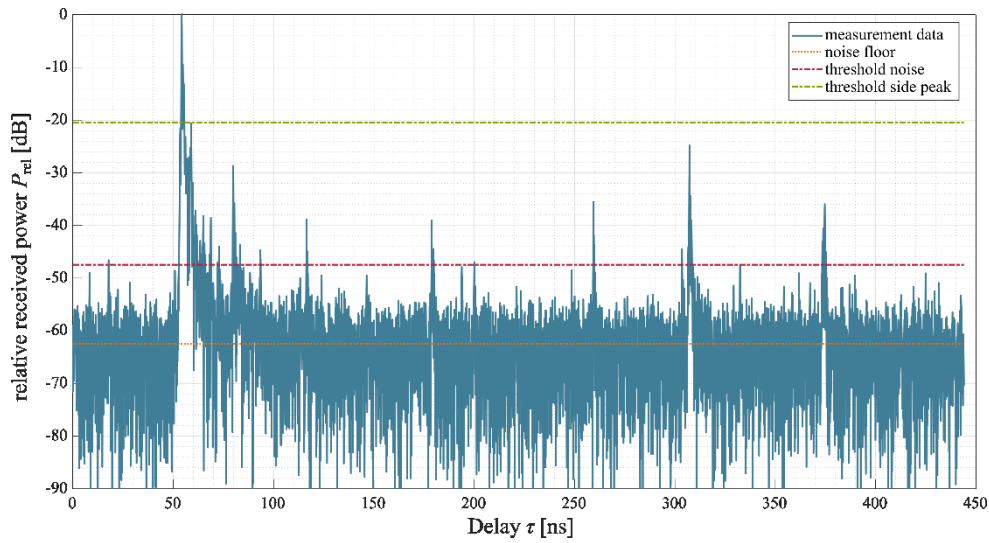


**Figure 10: Exemplary measurement with noise floor and threshold levels**

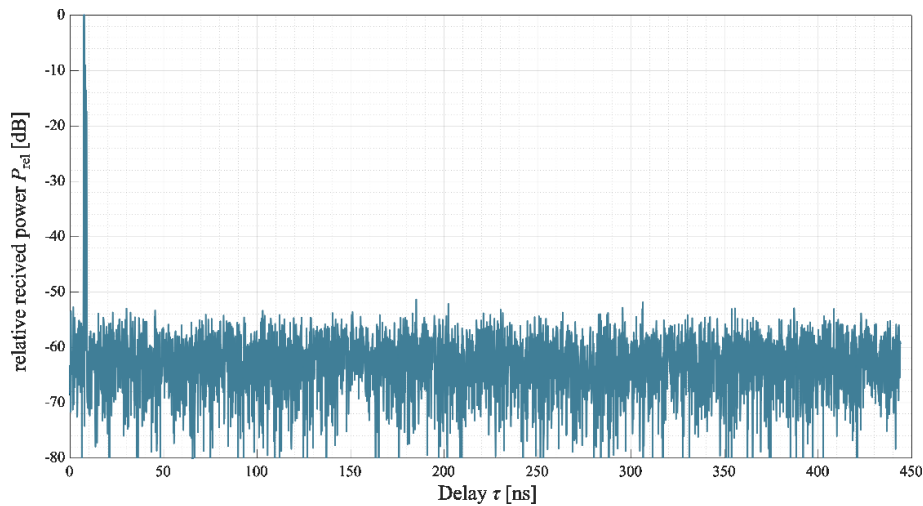


**Figure 11: Result after calibration**

## 2.3 Measurement Evaluation GUI

In order to simplify and making the process of analysing the channel sounder data more efficient, a MATLAB based Post Processing graphic user interface (GUI) was developed which is shown in Figure 12. The GUI can be separated into six different parts: Main Settings, Calibration, Plot Options, General Options, Power Delay Profile Options and Angular Profile Options.



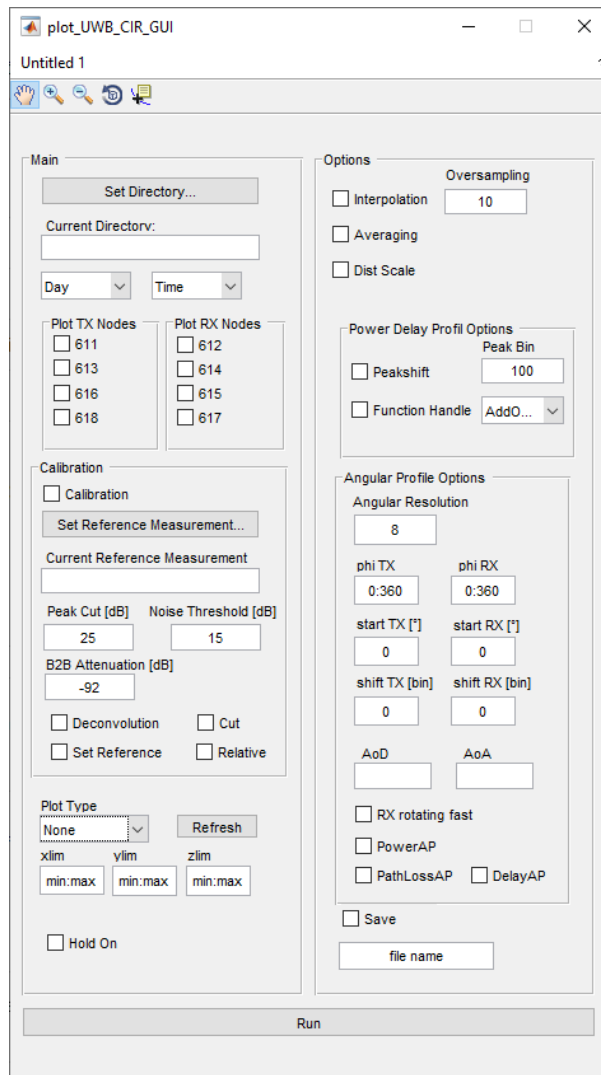


**Figure 12: Post-processing graphic user interface (GUI)**

The Main Settings are mandatory. They are used to choose the data set which should be plotted and analysed. After a directory that includes all relevant channel sounder generated data folders, set by pressing the “Set Directory” button, the current directory is displayed in the corresponding “Current Directory” text box. If needed, individual measurements can be chosen by setting appropriate day and time using the drop-down menus “Day” and “Time”. Finally the used sensor nodes have to be selected by checking the corresponding boxes “Plot TX Nodes” and “Plot RX Nodes”.

If requested, a calibration of the data can be performed before the data is plotted. Therefore the check-box “Calibration” has to be checked and a corresponding reference B2B measurement has to be set by pressing the button “Set Reference Measurement”. The chosen measurement is shown in the text box “Current Reference Measurement”. Within the post processing, the GUI provides two calibration methods which can be chosen by checking the related check-box: Deconvolution and Cut. If “Deconvolution” is set, a deconvolution as described in Section 2.2.2 is carried out. If “Cut” is set, a calibration as described in Section 2.2.3 is performed. Therefore the values and thresholds of “Peak Cut”, “Noise Threshold” and “B2B Attenuation” have to be set. Furthermore the data can be plotted in a normalized way relative to the highest amplitude. In this case the check-box “Relative” has to be checked. Also, a different measurement can be used as a reference. To select a measurement as reference the “Set Reference” is checked.

Apart from the calibration the main task of the post processing GUI is to plot the channel sounder data. Therefore the tool offers the following different plot types which can be chosen by the corresponding drop-down menu: Power Delay Profile (two- or three-dimensional corresponding to time invariant and



time variant, respectively), Power Spectrum (two- or three-dimensional), Angular Profile, omnidirectional CIR, Angular Power Delay Profile and Differential Plot. The Power Delay Profile shows the received power as a function of the delay for a single measurement (two-dimensional) or for a time variant series of measurements where the third dimension represents the different measurements. In the case of a single Power Delay Profile the corresponding delay spread of the measurement will be calculated and displayed. Similarly this applies to the Power Spectrum where the power is plotted as a function of the frequency. The Power Angular Profile shows the received power depending on the angle of arrival (AoA) and the angle of departure (AoD) where the third dimension represents the power. In this case the angular spread will also be calculated using the definition

$$\theta_{\text{spread}} = \sqrt{\frac{\sum_{k=1}^K \varphi_k^2 \cdot PDP(\varphi_k)}{\sum_{k=1}^K PDP(\varphi_k)} - \left( \frac{\sum_{k=1}^K \varphi_k \cdot PDP(\varphi_k)}{\sum_{k=1}^K PDP(\varphi_k)} \right)^2} \quad (2.14)$$

Due to the fact that the channel sounder measures the CIR with highly directive antennas, the omnidirectional CIR (ODCIR) of the channel can be calculated based on these spatial CIRs. The result is a superposition of the single CIRs calculated by

$$ODCIR = \sum_k |h_k(\tau_{max})|^2 \cdot \delta(\tau - \tau_{max}) + \sum_j |n_{Re} + j \cdot n_{Im}|^2 \cdot \delta(\tau - \tau_j) \quad (2.15)$$

where  $h$  denotes the CIR, and  $\delta$  is the Dirac delta function. The noise is generated synthetically and added after the superposition represented by the random variable  $n$  in the formula [8]. This programmed ODCIR function also offers to calculate the delay spread defined as

$$\tau_{\text{delay spread}} = \sqrt{\frac{\sum_{k=1}^K \tau_k^2 \cdot PDP(\tau_k)}{\sum_{k=1}^K PDP(\tau_k)} - \left( \frac{\sum_{k=1}^K \tau_k \cdot PDP(\tau_k)}{\sum_{k=1}^K PDP(\tau_k)} \right)^2} \quad (2.16)$$

The limits of the axes can be manually set to the values “xlim”, “ylim” and “zlim” by pressing the button “Refresh”. If more than one data set should be plotted in a single figure, the check-box “Hold on” has to be checked.

To modify the data the following options are available: “Interpolation”, “Averaging” and “Dist Scale”. If “Interpolation” is set, the data is interpolated by zero padding with the factor which is given by “Oversampling”. For each measurement the channel sounder records a programmable number of CIRs. By averaging the CIRs in a static scenario, the dynamic range of the channel sounder can be increased since white noise can be reduced. Within the options one can chose if the data should be averaged for each measuring point or not. Therefore the check-box “Averaging” has to be set. The “Dist Scale” option allows to transform the delay axes into distance axes using the speed of light. For analysis reasons this option is quite helpful to trace propagation and possible interactions points in the geometric environment where the measurement takes place.

More special options can be set within the Power Delay Profile Options and the Angular Profile Options. Regarding the Power Delay Profile, the main peak can be set manually to a certain peak bin. Therefore the check-box “Peakshift” and a peak bin has to be set. This allows direct comparison between power delay profiles even if they have different delays. The Function Handle option is the interface to newly developed functions that can easily be used without being implemented in the GUI.

If various spatial measurements should be analysed/plotted together as Angular Profile, the Angular Profile Options are mandatory. Here the Angular Resolution and the covered range of the TX (“phiTX”) and of the RX (“phiRX”) in azimuth have to be set in accordance with the chosen measurement. If a





transformation of the coordinate system is necessary, as for example for the comparison of the measurements with simulations, results offset can be set by startTX, startRX. In addition, an arbitrary shift can be added by setting shiftTX and shiftRX. During rotational measurements one node is rotated in an inner loop while the other node is rotated in an outer loop. The node which is rotated in the inner loop makes a full rotation for each step of the outer loop. Therefore the node of the inner loop rotates more often or “faster” than the node of the outer loop. In order to interpret the measured data in the correct order it has to be determined if the TX or the RX is the node in the inner and outer loop, respectively. Normally the TX is the node in the inner loop. If not, the check-box “RX rotating fast” has to be checked. Finally the user can choose which values should be plotted in the angular profile by checking the corresponding check-box: received power, path loss or delay.

When all settings have been made the plot can be generated by pressing the button “Run”. If desired the plot and the corresponding data can be saved as a figure and a mat-file by giving a file name and checking the check-box “Save”.

## 2.4 Inter-rack Measurements

In this section, the inter-rack measurements are analysed and important characteristics such as the delay spread and the angular spread are presented. As explained in section 2.1 the inter-rack measurements are grouped into general characterisation (GC) which will be presented first and top-of-rack (ToR) measurements which follow afterwards.

The first set of measurements aim at investigating general reflection and propagation effects in a data centre and analyse the specific data centre environment with the typical layout with racks placed in rows at a certain distance. In this set of four GC FO rotational measurements TX and RX are always positioned in the same aisle in the data centre and at a height of 1.50 m. We recall the setups described in detail in the deliverable D4.3 in Table 2.

**Table 2: List of GC FO setups**

identifier	$d/m$	$\vartheta_{TX}/^\circ C$	$\vartheta_{RX}/^\circ C$	polarisation
GC FO long cold vertical lcv	12.52	26.6	26.6	vertical
GC FO short cold vertical scv	3.66	26.6	26.6	vertical
GC FO short cold horizontal sch	3.66	26.6	26.6	horizontal
GC FO long hot vertical lhv	12.47	30.4	30.4	vertical

GC FO lcv shows TX and RX at a distance of 12.52 m and GC02 at a distance of 3.66 m. The omnidirectional channel IRs (ODCIRs) are plotted in Figure 13 and Figure 14, respectively. For the whole section the measurement accuracy for the path loss stays in the order of  $\pm 1$  dB. The value is based on the authors experience with the measurement equipment. The delay accuracy is assumed to be  $\pm 0.3$  ns.



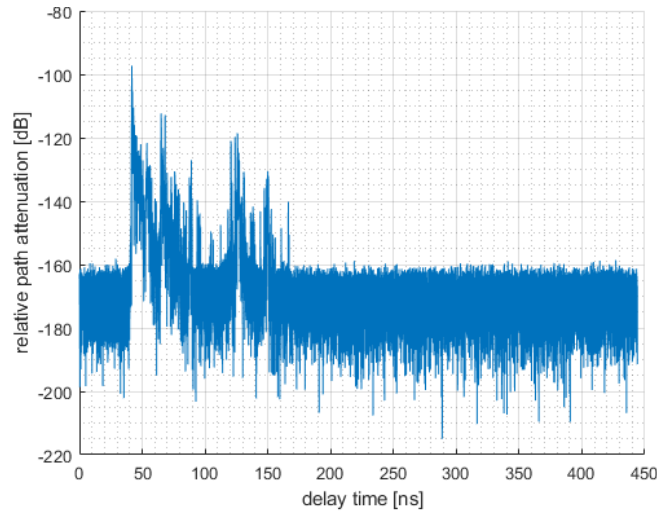


**Figure 13: Omnidirectional channel impulse response of GC lcv**

It is obvious that the delay of the direct path is reduced for the shorter distance. Both path loss and delay agree well with the FSPL model as already presented in D4.3 and in both cases the direct path represents the strongest MPC.

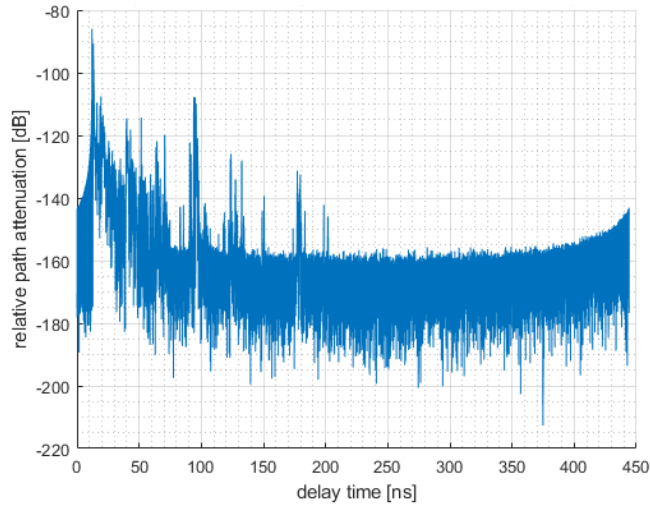


**Figure 14: ODCIR of GC FO scv**

Both IRs have also in common that a dense and decreasing floor of lower MPCs follow the direct path up to an excess delay of 50 ns. The maximum excess delay of a MPC is 125 ns for the long distance in GC FO lcv and 189 ns for the short distance in GC FO scv. In the first case with a long distance between TX and RX the first reflected MPC occurs at an excess delay of 0.41 ns with an additional path loss of 7.82 dB. In the second case with short distance between TX and RX, the first reflected MPC occurs at 0.97 ns with an additional path loss of 4.69 dB. Other striking MPCs are listed in Table 3. Both setups have in common that only one MPC exists with additional path loss below 10 dB and a number of MPCs occur at an excess delay of around 80 ns. For the short distance measurement all other MPCs are even below 20 dB of additional path loss. Also remarkable is the large gap between 7 ns and 80 ns where only lower MPCs occur.

**Table 3: Striking MPCs of GC FO lcv and GC FO scv**

	GC FO lcv		GC FO scv	
No.	Additional PL [dB]	Excess delay [ns]	Additional PL [dB]	Excess delay [ns]
1	7.8	0.41	4.7	0.97
2	15.4	23.28	23.5	3.89





3	15.4	26.45	24.5	6.44
4	24.3	78.88	21.5	7.14
5	22.5	82.18	21.8	81.88
6	21.3	84.08	21.8	82.85

The next measurement aims at investigating the influence of polarisation. We will therefore point out the differences between GC FO scv with vertical polarisation and GC FO sch with horizontal polarisation, the ODCIR of which is plotted in Figure 15

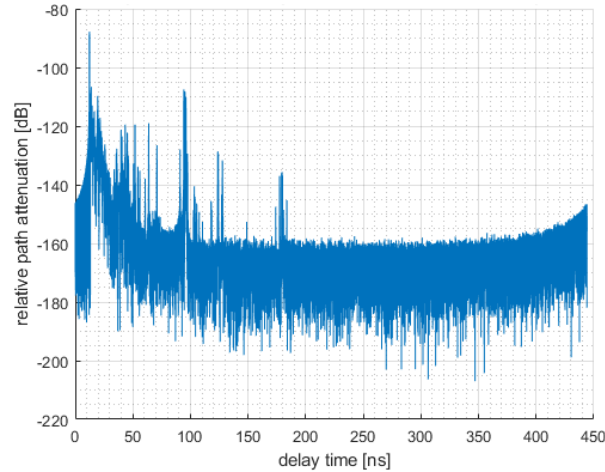


**Figure 15: ODCIR of GC FO sch**

In general the MPCs have a higher additional PL for the horizontal polarisation of around 5 dB which can be explained by the different reflection coefficients for the respective polarisation. Here, the important MPC at an excess delay of 0.97 undergoes the biggest difference with a higher additional loss of 14.02 dB. Table 4 summarises the MPCs of the horizontal polarised measurement and compares the additional path loss with the vertical polarised measurement where

$$PL_{\text{diff}} = PL_{\text{horizontal}} - PL_{\text{vertical}}$$

In contrast to the much attenuated MPC at 0.97 ns, the MPCs at around 80 ns are not influenced very much. They rather show a weaker attenuation which could stay within the measurement tolerance.

**Table 4: Polarisation dependent comparison of the path loss**

No.	Additional PL of GC FO sch [dB]	Difference to GC FO scv [dB]
1	18.7	14.0
2	27.2	3.7
3	26.7	2.2
4	21.8	0.3
5	19.6	-2.2
6	20.4	-1.4

The last measurement of the GC set was performed in a hot aisle and with a long distance between TX and RX where the main difference with GC FO lcv aside from the temperature was the fact that all racks were placed with their rear sides pointing into the aisle. The rear side of a rack is more flat and has more metal parts without holes. It can be assumed that the rear side can be modelled more easily by a flat metal plate as compared with the front part of the rack. The ODCIR plotted in Figure 16 appears more compressed and dense. The major part of all MPCs lies within the above mentioned decreasing floor up to an excess delay of 59 ns. Only one cluster is present beyond this value at an excess delay of 82.9 ns



which was already observable in the discussed measurements but has in this case a higher additional attenuation of 33.5 dB. Another remarkable fact is that the direct path is followed by six strong MPCs that seem to have at least the same or higher power than the direct path which might be due to a superposition of various paths with the same delay. As a conclusion, one could say that the data centre geometry leads to a rich multi path environment and that the rear sides of the racks encourage reflections such that they may influence or inhibit communications due to inter symbol interference.

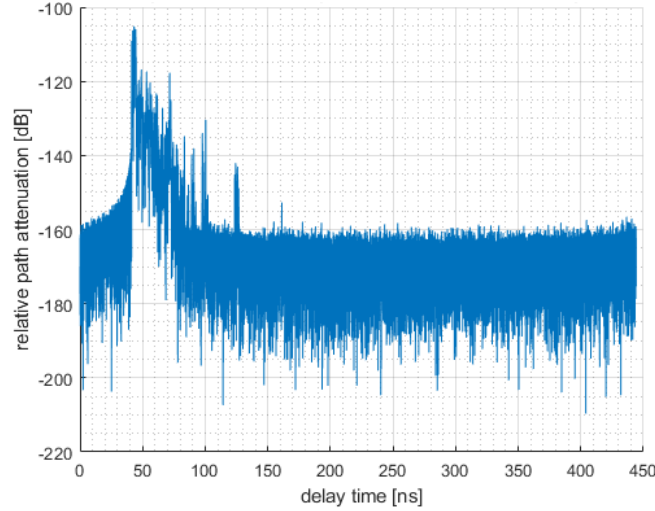


**Figure 16: ODCIR of GC FO lhv**

The top-of-rack investigations refer to the most likely application scenario of wireless top-of-rack links that connect two racks with each other. Since the data traffic within one rack is often steered by the top-of-rack switch, also the physical position of the antenna on the top of the rack makes sense. Table 5 recalls the scenarios presented in D4.3.

**Table 5: List of ToR FO setups**

identifier	$d/m$	$\vartheta_{TX}/^\circ C$	$\vartheta_{RX}/^\circ C$	polarisation
ToR FO same aisle vertical sav	3.68	26.6	26.6	vertical
ToR FO adjacent aisle vertical aav	4.56	30.4	26.6	vertical
ToR FO aisle vertical horizontal aah	4.56	30.4	26.6	horizontal
ToR FO next to adjacent aisle vertical ntaav	7.33	21.9	26.6	vertical
ToR FO next to adjacent aisle horizontal ntaah	7.33	21.9	26.6	horizontal

Beginning with the setup where TX and RX are located in the same aisle, it can be observed that the ODCIR presented in Figure 17 can be divided into two parts. The first part up to an excess delay of 83 ns can be characterised by many MPCs at a regular distance with an additional path loss between 21.12 dB and 42.92 dB and a delay difference of 6 ns to 10 ns. In the second part after 83 ns only five MPCs occur with a significant higher path loss. Compared to the GC measurements, one can see a certain similarity that might be due to the fact that the reflections from the racks are replaced by reflections from the plastic curtains that are located above every row of racks. However, the most interesting part is located directly beyond the direct path where multiple MPCs overlap, resulting in a MPC with 3.05 dB less path loss than the direct path. This cluster of MPCs may influence the wireless link strongly, potentially causing self-interference and ISI.



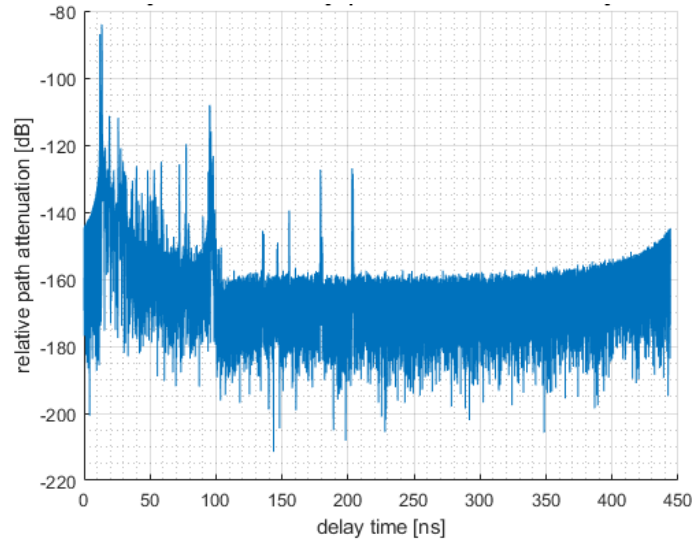


**Figure 17: ODCIR of ToR sav**

Placing RX in the adjacent aisle, we note that the first part with a high density of MPCs already ends at an excess delay of 30 ns. Only two MPCs beside the direct path have a lower additional path attenuation than 20 dB, namely 16 dB and 14.1 dB at an excess delay of 21.01 ns and 55.5 ns, respectively. The situation of the direct path is more relaxed since it dominates all other MPCs by at least 14.1 dB.

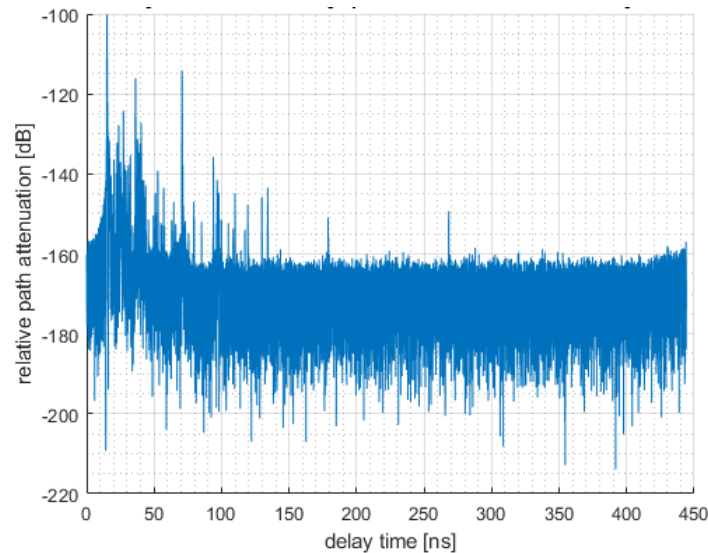


**Figure 18: ODCIR of ToR aav**

The comparison between the vertical polarisation in Figure 18 and the horizontal polarisation in Figure 19 shows that the direct path is attenuated in the same way but other paths are affected by an increase or decrease of the path loss. One can note that all paths which are present in the horizontal case are also present in the vertical case. The other way around does not hold true especially after an excess delay of 82.25 ns where the IR with horizontal polarisation does not show any MPCs. One of the two above mentioned striking MPCs at an excess delay of 21.01 ns is more attenuated and the other at an excess delay of 55.5 ns is less attenuated resulting in an additional attenuation of this MPC of only 4.00 dB.



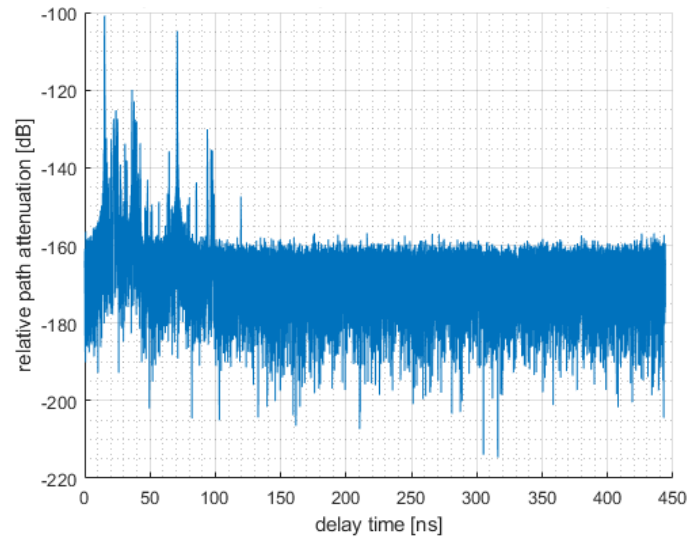


**Figure 19: ODCIR of ToR aah**

Increasing the distance even further to the next-to-adjacent aisle, it can be seen that the number of MPCs and their impact decreases drastically. The highest MPC beside the direct path has an additional attenuation of 27.3 dB for the vertical polarisation illustrated in Figure 20 and 27.5 dB for the horizontal polarisation plotted in Figure 21.

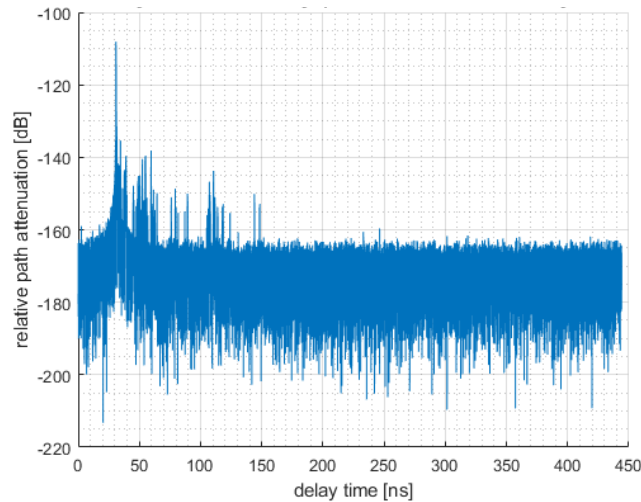


**Figure 20: ODCIR of ToR ntaav**

As for the adjacent aisle setup before, some MPCs that are present in the vertical polarisation case disappear in the horizontal polarisation case. For example, the maximum access delay in the vertical measurement is 117.51 ns whereas the horizontal measurement shows a maximum delay of 93.27 ns. Those MPCs that exist in both measurements can easily be matched to each other and their difference in path loss stays within an interval of 5 dB.



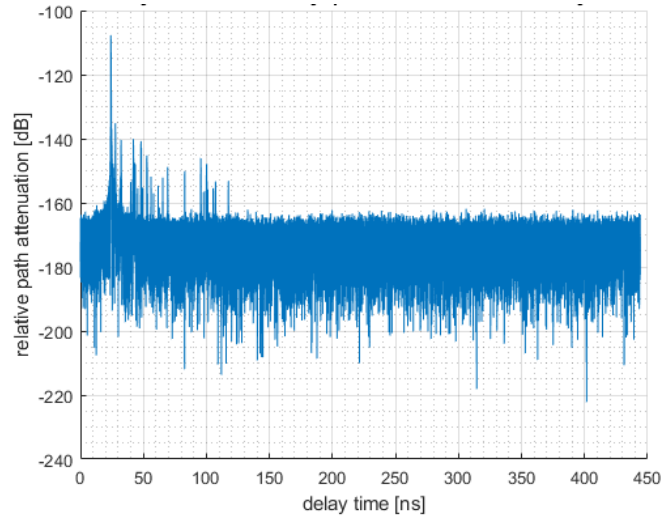


**Figure 21: ODCIR of ToR ntaah**

To further quantify the characteristics of the respective measurements, the RMS delay spread can be analysed. Table 6 collects all delay spreads of the FO measurements. We note that all delay spreads of the GC measurements in the cold aisle characterised by the front of the racks are placed around 11 ns. As discussed before, the IR in the hot aisle with the rear side of the racks is compressed and dense, which is also reflected in the shorter delay spread. Many MPCs with high amplitude and low delay lead to a delay spread of 5.06 ns.

The delay spread of the ToR scenarios is low for short distances, increases for medium distances and decreases again for long distances. This effect can be explained by the fact that for short distances the direct path and some MPCs with a short delay dominate. For the medium distance, where the direct path is also attenuated by transmission through the plastic curtains, the influence of MPCs with higher delays increases. Finally, for the long distance, no MPCs exist that have a high influence. So only the direct path dominates leading to a short delay spread.

**Table 6: Delay spread and angular spread of all FO measurements**

Identifier	RMS delay spread [ns]	AoD spread [°]	AoA spread [°]
GC FO lcv	11.6	25.4	29.8
GC FO scv	11.5	25.3	26.6
GC FO sch	10.6	22.6	25.1
GC FO lhv	5.1	15.5	43.9
ToR FO sav	6.6	22.0	17.0
ToR FO aav	10.4	11.8	24.7
ToR FO aah	24.6	15.0	27.4
ToR FO ntaav	3.1	8.7	12.0
ToR FO ntaah	2.0	12.5	11.4

Not only temporal aspects play an important role for wireless links in a DC but also spatial characteristics. Since sub-THz communication will likely be implemented as a point-to-point link, directive antennas will be used to overcome the higher FSPL and the low output power of THz transmitters. The FO measurements were performed with a standard directive gain horn antenna serving as a spatial filter, enabling an analysis of spatial characteristics and the angular spread.



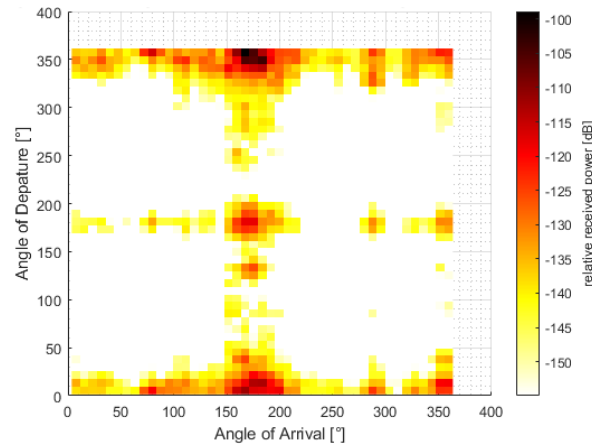


**Figure 22: PAP of GC FO lcv**

Starting with the GC measurements, the power angular profile (PAP) of GC FO lcv is presented in Figure 22. The coordinate system is adapted to the one from the data centre model where the x-axis is oriented in the direction of the main corridor and the y-axis along the aisles with the rows of racks (see section 3.2). The direct path is located at an AoD of  $357.5^\circ$  and an AoA of  $175.5^\circ$ . The strongest MPCs can be found at small angles around the direct path. In general, power was received for all AoAs at an AoD of  $357.5^\circ$  and for many AoAs at an AoD of around  $180^\circ$ . In addition, many AoDs lead also to a received signal at an AoA around  $175^\circ$  resulting in a cross-shaped figure with clear white spaces.

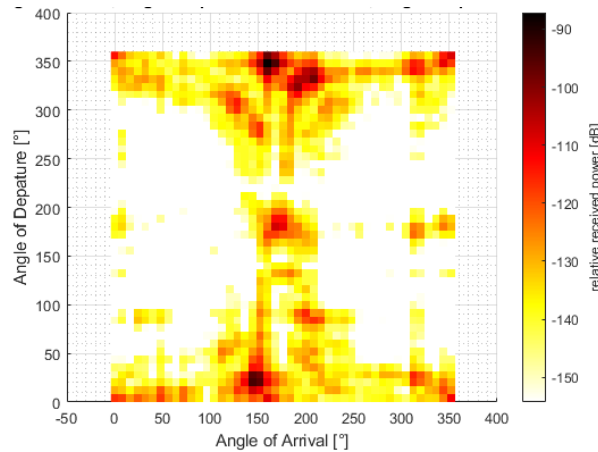


**Figure 23: PAP of GC FO scv**

A similar picture is obtained for the PAP of GC FO scv illustrated in Figure 23. It is notable that more power is received from greater relative angles with respect to the direct path. Compared with the changes in the environment this difference makes sense because the relative AoDs and AoAs increase for the same reflection points at the front of the rack. However, the influence of this effect is not sufficiently important that the angular spread is also affected. The comparison of the vertical and horizontal polarisation (Figure 23 and Figure 24) visualises especially the influence of the horn antenna that has high side lobes for horizontal polarisation and low side lobes for vertical polarisation. Therefore the PAP in Figure 24 seems to be blurred. On the other hand, the antenna gain is independent of the polarisation and therefore it is not due to the antenna that MPCs have a lower amplitude for the horizontal polarisation, but to the reflection and propagation behaviour itself. So the MPCs at (AoD|AoA)  $(28^\circ|144^\circ)$ ,  $(324^\circ|192^\circ)$  and  $(332^\circ|208^\circ)$  are around 14 dB lower for horizontal polarisation. This compensates for the fact of the blurred PAP, and the angular spread stays almost constant. Removing the impairments of the antenna would result in a lower angular spread for horizontal polarisation.



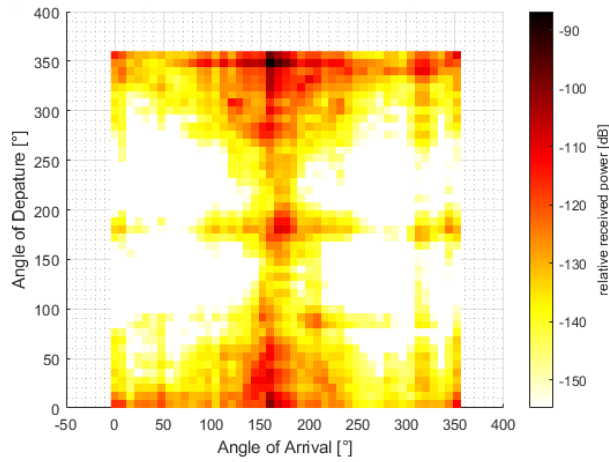


**Figure 24: PAP of GC FO sch**

The above mentioned measurements showed a circular placement of the MPCs around the direct path. The PDP of the measurement in the hot aisle shown in Figure 25 has a lower dependency on the AoD and the majority of the MPCs are located at the AoD of the direct path of  $2^\circ$ . This is also visible in the angular spread where the angular spread of the AoD decreases to  $15.45^\circ$  and the angular spread of the AoA increases to  $43.86^\circ$  which is mainly due to the MPCs at  $(2^\circ|79.5^\circ)$ .

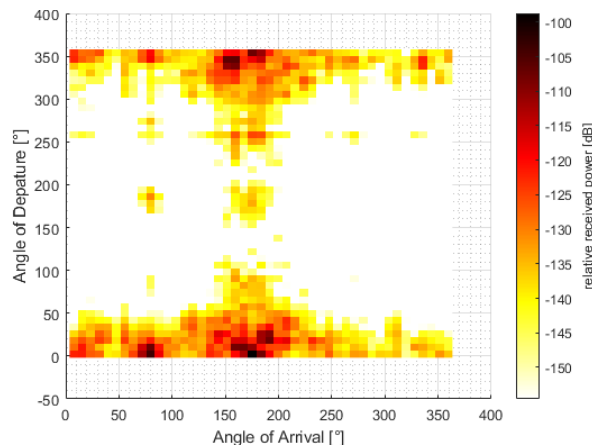


**Figure 25: PAP of GC FO lhv**

The top-of-rack scenarios are characterised by a lower number of MPCs that are more spread around the room. An interesting fact of the PAP of the measurement in the same aisle plotted in Figure 26 is that the first reflected path has only an additional path attenuation of 2.84 dB at a relative angle of  $(40^\circ|16^\circ)$ . In combination with side lobes from steerable antenna arrays this may lead to strong multipath effects like inter-symbol interference.



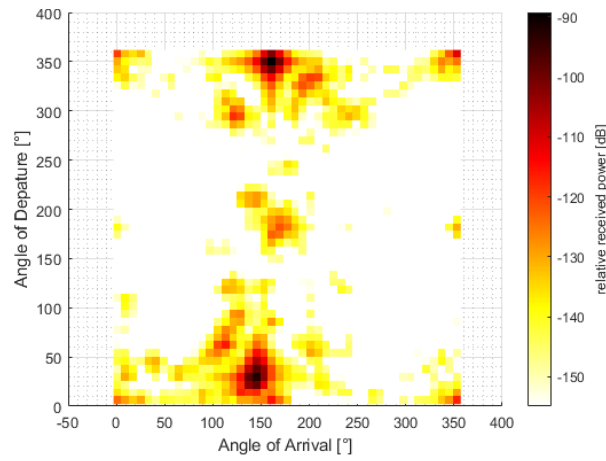


**Figure 26: PAP of ToR FO sav**

With increasing distance the amount of strong paths decreases. Figure 27 and Figure 28 show the adjacent aisle measurement where for both polarisations the same MPCs were measured. Again, the influence of the antenna pattern is very present.

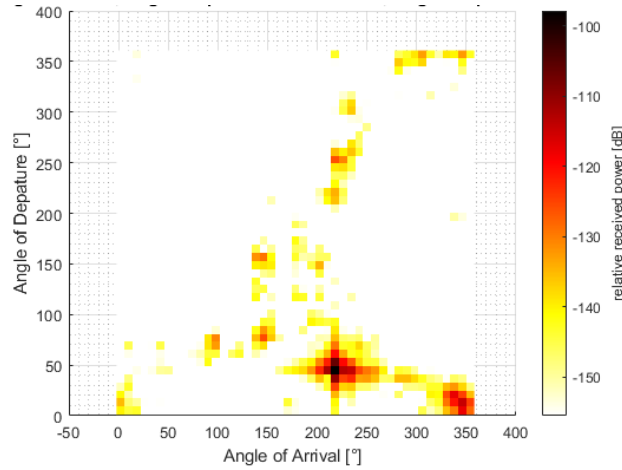


**Figure 27: PAP of ToR FO aav**

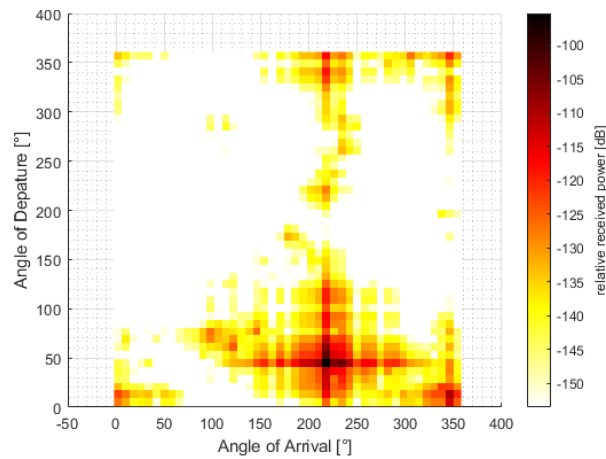


**Figure 28: PAP of ToR FO aah**

The next-to-adjacent aisle measurement in Figure 29 and Figure 30 finally show that the direct path is the dominant part for an increased distance, and MPCs play a negligible role. In general one could conclude that it is favourable from the perspective of the channel to have communication over a longer distance with TX and RX not positioned in the same aisle. On the one hand, transmission through the





curtains adds an additional loss but on the other hand the number of interfering MPCs reduces significantly.

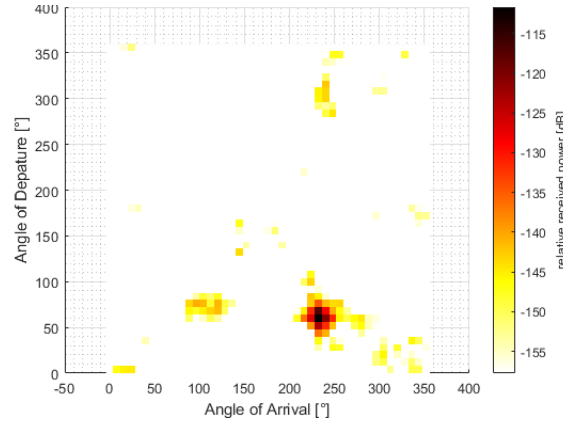


**Figure 29: PAP of ToR FO ntaav**

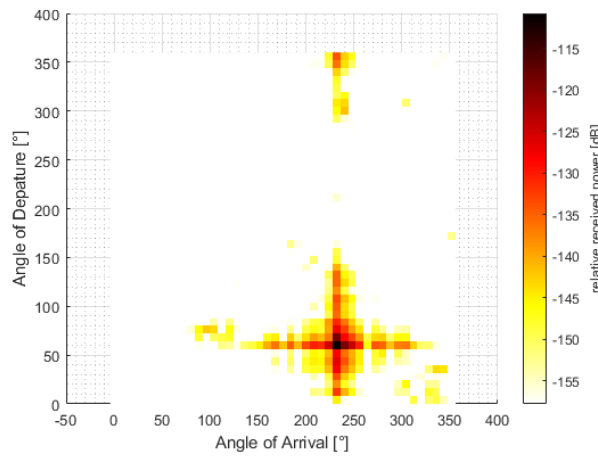


**Figure 30: PAP of ToR FO ntaah**

## 2.5 Intra-rack Measurements

Another component of wireless links in DC are the intra-rack links. These links connect two servers in the same rack. The difficulty in this scenario is that the rack with its metal corpus is a good reflector. Strong multipath components could inhibit good communication in the rack. This section investigates the impulse response for intra rack communication. Therefore the measurement setups emulate a likely intra-rack link between two servers in a metal rack with a height of 1.95 m, a width of 0.603 m and a depth of 1.09 m. The RX is attached to a holding device and mounted at the highest position in the rack such that the antenna is positioned at a height of 1.59 m. It is faced downwards such that the antenna points to the floor with an elevation angle of  $171^\circ$  in spherical coordinates. The TX is mounted on top of a tripod and faced upwards with an elevation angle of  $13^\circ$ . TX and RX both use a standard gain horn antenna with a gain of 15 dBi and a HPBW of  $35^\circ$ . Three different antenna heights of the TX are investigated each with a different number of servers in the rack. First, TX is positioned at the highest position (shortest distance) where only one server fits in between TX and RX. Then, TX is moved to the medium distance and the number of servers is increased stepwise to the maximum number of servers that fits in between TX and RX. After that, TX is moved to the lowest position with the greatest distance and the number of servers is increased again. Finally, all servers are removed one after the other. Figure 31 illustrates the measurement setup with the three different distances. The measurements are performed with the rack doors closed so that reflections from all rack parts will be visible. Only for further investigations in measurements No. 15, 16 and 17 the doors are opened, and in No. 17 absorbers are



also installed to investigate the influence of the rack cabin. Table 7 gives a comprehensive overview of all performed intra-rack measurements.

**Table 7: Intra-rack measurement setups**

No.	TX position [m]	RX position [m]	Distance	No. of servers	remark
1	(0.30, 0.817, 1.29)	(0.36, 0.882, 1.59)	short	1	
2	(0.256, 0.852, 0.965)	(0.36, 0.882, 1.59)	middle	1	
3	(0.256, 0.852, 0.965)	(0.36, 0.882, 1.59)	middle	2	
4	(0.256, 0.852, 0.965)	(0.36, 0.882, 1.59)	middle	3	
5	(0.256, 0.852, 0.965)	(0.36, 0.882, 1.59)	middle	4	
6	(0.22, 0.841, 0.605)	(0.36, 0.882, 1.59)	long	4	
7	(0.22, 0.841, 0.605)	(0.36, 0.882, 1.59)	long	5	
8	(0.22, 0.841, 0.605)	(0.36, 0.882, 1.59)	long	6	
9	(0.22, 0.841, 0.605)	(0.36, 0.882, 1.59)	long	5	idem to 7
10	(0.22, 0.841, 0.605)	(0.36, 0.882, 1.59)	long	4	idem to 6
11	(0.22, 0.841, 0.605)	(0.36, 0.882, 1.59)	long	3	
12	(0.22, 0.841, 0.605)	(0.36, 0.882, 1.59)	long	2	
13	(0.22, 0.841, 0.605)	(0.36, 0.882, 1.59)	long	1	
14	(0.22, 0.841, 0.605)	(0.36, 0.882, 1.59)	long	0	
15	(0.22, 0.841, 0.605)	(0.36, 0.882, 1.59)	long	0	back door open
16	(0.22, 0.841, 0.605)	(0.36, 0.882, 1.59)	long	0	front door open
17	(0.22, 0.841, 0.605)	(0.36, 0.882, 1.59)	long	0	with absorbers



**Figure 31: Measurement setup of the Intra-rack measurement; left: short distance, middle: medium distance, right: long distance**



All measurements show that the direct path represents the strongest component in the impulse response. This can be clearly seen in Figure 32 where measurement No. 1 is compared with the B2B calibration measurement. Several MPC are visible up to a delay of 35 ns. All peaks with a delay greater than 35 ns have a corresponding peak in the B2B measurement and therefore originate from the channel sounder system itself. Therefore, the IR for all intra-rack measurements will be cut at 35 ns for further post processing such as the calculation of the delay spread.

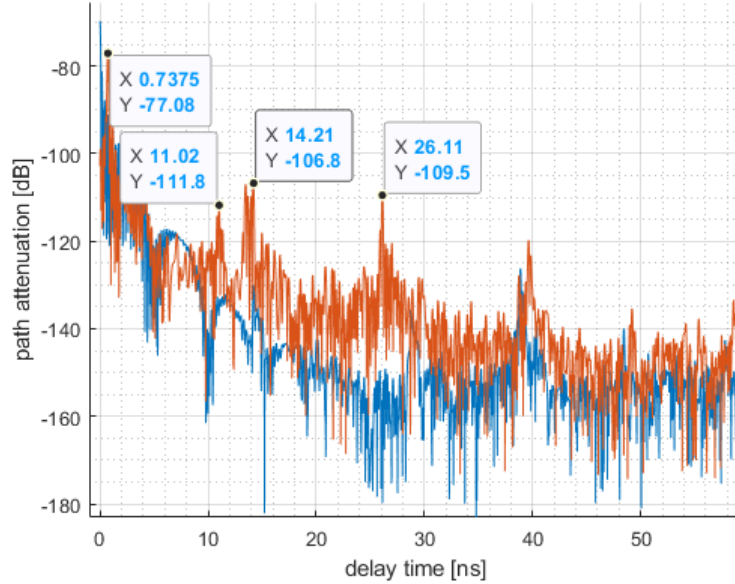


**Figure 32: IR of the B2B measurement (blue) and the Intra-rack measurement No. 01 (orange)**

The IR of measurement No. 1 shows overall four remarkable peaks at 0.73 ns, 11.02 ns, 14.21 ns and 26.11 ns, respectively. For all measurements it can be stated that the direct path is very close to the theoretical free space path loss (FSPL) as summarised in Table 8. Furthermore, no direct relation between the number of servers and the path loss of the direct path can be observed since the PL of No. 8 with the maximum number of servers is not higher than No. 14 without any server. This result was expected since the servers do not block the direct path and all measurements are done in a LOS scenario. Regarding the delay, it is observable that the measured delay of the direct path is always 0.3 ns – 0.4 ns lower than the theoretical delay calculated by the distance and the speed of light. We can therefore assume a systematic error in the measurements due to an imprecise calibration. Since the deviation is constant, further analysis like the delay spread are not affected.

**Table 8: Direct path characteristics of intra-rack measurements**

No	PL direct path [dB]	delay direct path [ns]	FSPL [dB]	theoretical delay [ns]	delay spread [ns]
1	-77,1	0,73	-71,89	1,04	1,13
2	-79,9	1,81	-78,03	2,11	1,09
3	-79,5	1,79	-78,03	2,11	1,18
4	-79,3	1,83	-78,03	2,11	1,22
5	-82,3	1,82	-78,03	2,11	1,62
6	-84,1	2,94	-81,95	3,32	2,29
7	-81,8	2,93	-81,95	3,32	1,32
8	-83,9	2,94	-81,95	3,32	1,41
9	-81,9	2,94	-81,95	3,32	1,43
10	-84,7	2,92	-81,95	3,32	2,20



11	-84,5	2,90	-81,95	3,32	1,99
12	-84,0	2,89	-81,95	3,32	1,72
13	-85,5	2,86	-81,95	3,32	2,03
14	-86,8	2,84	-81,95	3,32	2,23
15	-85,5	2,85	-81,95	3,32	1,96
16	-84,2	2,89	-81,95	3,32	1,72
17	-83,7	2,90	-81,95	3,32	0,97

The main findings will be illustrated by the exemplary comparison of No. 6 and No. 17 which show the greatest and the lowest delay spread respectively. In setup No. 6, TX and RX have the longest distance and four servers in between. Setup No. 17 shows also the longest distance but has no servers, opened doors and attenuators on the bottom of the rack cabin. Both setups are shown in Figure 33 and their IRs are plotted in Figure 34 where No. 6 is illustrated in blue and No. 17 is illustrated in orange.



**Figure 33 Measurement setup No. 6 (left) and No. 17 (right)**





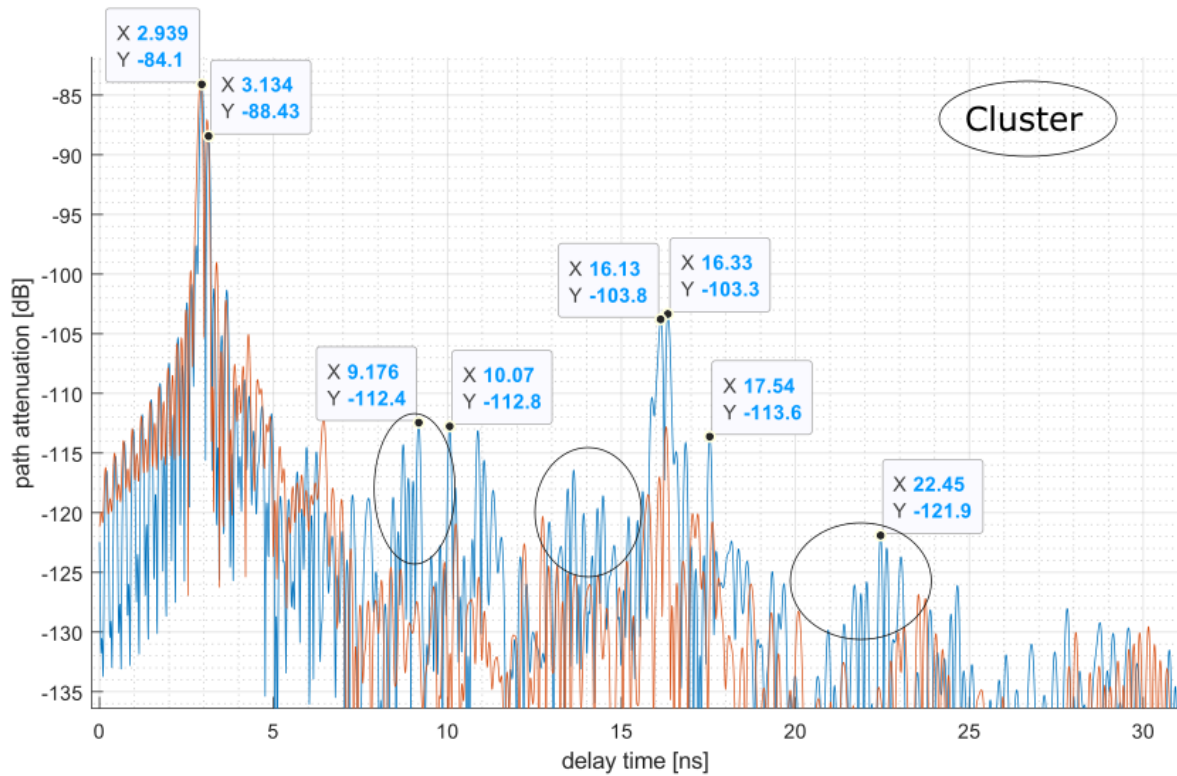


**Figure 34: IR of measurement No. 6 (blue) and No. 17 (orange)**

It can be noted that the direct path and first strong peak at 3.13 ns which could be a reflection from the rack's side wall are not affected by the number of servers nor the doors or the ground strut. However, there are some differences in the impulse response at a greater delay that originate from two effects. The first effect is the influence of the rack cabin itself noted in the striking peak at 16.13 ns which is due to a reflection from the rack's ground strut. An additional attenuation of this MPC by -10 dB was achieved by the absorbers on the ground. All measurements without absorbers show this strong component at 16.13 ns. The second effect can be related to the servers. The servers which don't block the direct path introduce a various number of weak MPCs starting at a delay of 6.5 ns. These MPCs appear in groups and are marked with a circle. The number of MPCs is not directly linked to the number of servers because the delay spread does not show a direct relation to the number of servers. A possible model could be a cluster based approach that creates a certain number of MPCs at a certain delay based on the presence of servers. However, the influence of the servers plays a minor role compared to the intrinsic characteristics of the rack cabin since the highest MPC is still 10 dB below the rack cabin's MPC. This might be due to the already spatially filtered impulse response where the horn antenna strongly attenuates MPCs with high angles of departure and arrival. This effect might even be stronger with antennas with higher directivity which will likely be used in a real application. In addition, interference effects from other intra-rack links which simultaneously transmit data were not part of this investigation and could have a disadvantageous impact on the link performance.

To conclude the intra-rack measurements, it can be stated that the direct path of intra-rack links in a LOS condition agrees with the FSPL model. The distance of TX and RX does not substantially influence the number of MPC and the delay spread stays in the same order of magnitude. Main influences can be expected from the rack cabin itself and the interference from other links.



### 3 Channel Simulations

In the previous chapter 2, the real campaign of channel measurement has been handled. The evaluated results of measurement are used as basic information for the real-like simulations since it is one of the cost effective and time saving methods to predict on-site performances of the system. Furthermore, using simulation, it is also possible to formally gather the know-hows, information and prospects about the target environments and the propagation characteristics of the implemented system including interference level of each device. This allows to reduce effort of designing system and the probability of system failure, and is a means of optimizing system-planning, considering previously detected and foreseeable problems, conflicts and troubles.

For this reason, this chapter introduces the channel simulations related to the measurement campaign that is contained in chapter 2. To begin, section 3.1 contains a general description of the ray tracing simulation available at TUBS' mobile network simulator (SiMoNe)[9]. In the following section 3.2, the creation of the detailed 3D model of the Dell EMC Research Data Centre is described. Afterwards, the procedure of calibration of material parameters is introduced in section 3.3. Finally, in the section 3.4, propagation channel is modelled such by means of a stochastic model using ray-tracing simulation results.

#### 3.1 Ray-Tracing Simulations

It is obvious that real like simulations depend on how similar the modelling of simulation has been to real setup and how exact existing phenomenon have been realized. In this sense, a mobile network simulator, so called SiMoNe, is available at TUBS. It has been internally developed by the mobile radio systems group at TUBS, originally for simulating hundreds of base stations and thousands of mobile users [9]. The basic function of SiMoNe is a module based system. Which means, the entire complex computation is divided into smaller modules, so called functional blocks illustrated in Figure 35, and these blocks are concatenated to achieve different types of targets while maintaining the degree of freedom of constructing simulations. One of the elemental function of the network simulator is to find out existing rays between transmitters and receivers.

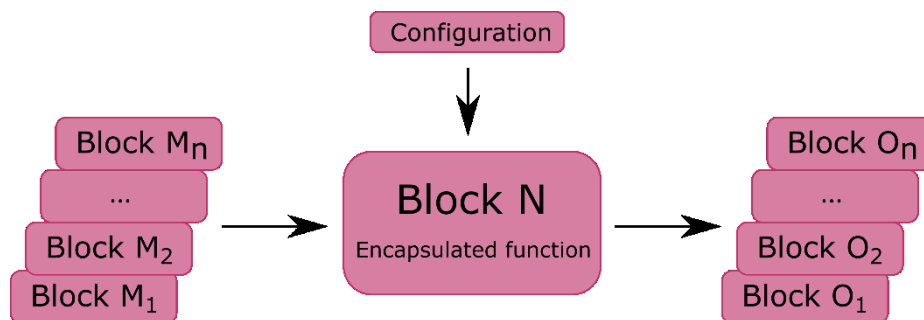


**Figure 35: Functional Block of SiMoNe**

As was briefly mentioned in the previous section, the main purpose of software simulation in mobile network field is to derive results as similar as possible to propagation results that are likely in the real environment. To accomplish this task, 3D ray tracing method is available by using SiMoNe considering 3D Building models. Additionally, atmospheric conditions including temperature, air pressure and humidity can be also accounted for in the calculation according to the operator's preference. Besides, our ray tracer can take into account several relevant propagation effects such as transmission, reflection, diffraction and scattering [11]. For computing each propagation effect, manifold well-known theories are available such as Fresnel coefficients method and transfer matrix method, especially for reflection.



The overall computation of 3D ray tracing method starts with searching for possible existing rays. First, SiMoNe updates the building source and obstacles on the basis of input specifications, e.g., which types and how many times propagation effects should be considered. Afterwards, it is initiated to find existing rays. While doing this, especially searching for reflected rays, image source method considering specular angles is used, described in further detail in [10]. During this computational step, transverse electric (TE) and transverse magnetic (TM) waves are separately computed and merged in a constructive or destructive manner considering their phase. Once all rays are detected, the radiation pattern of antenna is applied to each of the detected rays using the linear interpolation method. As the outcome of ray tracing, the following results are obtainable: e.g. Amplitude of TE and TM, delay spread, angle of arrival (AoA), angle of departure (AoD) and interaction points.

### 3.2 3D Model Building

In order to model a 3D version of the measurement environment the environment was mapped very precisely and in detail during the measurement campaign. In addition to that, the notes are supplemented by corresponding photos of the environment. Based on this data the environment itself and the objects within the environment are modelled, and finally the whole 3D Model is arranged with this individual models. Figure 36 exemplarily shows a photo of a sever rack on the left side and the Building 3D Model of this server rack on the right side.



**Figure 36: Dell EMC Unity All Flash Photo (left) and 3D Model (right)**

Within the simulator the model is organized as follows: Each object is built of individual surfaces. All surfaces of an individual object together are stored in a list of surfaces and used to build a Building 3D Model. Different Building 3D Models together, in turn, are stored in a list of Building 3D Models and used to build a Building 3D Collection.

To make the process and the models as generic as possible an importer was developed that generates different Building 3D Models based on a csv-file. Therefore the surfaces of a Building 3D Model are composed by generic algorithms using the values given by the csv-file. Table 9 shows the parameters of the csv-file and a short description of each parameter. It should be noted that these parameters are organized in columns in the csv-file in contrast to the shown arrangement in Table 9.

**Table 9: Generic Importer CSV-File Parameters**

Parameter	Description
Area Category	Identifier for different areas that includes different models, e.g. racks in the area “Data Centre” or tables in the area “Office”.



Main & Sub Category	Main Category identifies the object within the chosen area which should be generated, e.g. a rack or a table. The Sub Category specifies the chosen object, e.g. rack with door or without door, etc.
Model Name	Each Building 3D Model which is generated by the csv-file must have an individual name, e.g. "Rack_1" and "Rack_2" for two different racks.
X- / Y- / Z- Position	Gives the x-, y-, z-position of the Building 3D Model.
X- / Y- / Z- Direction (Width)	Gives the vector that defines the direction of the "Width". The direction vector of the width and the depth together define the orientation of the Building 3D Model in the room.
X- / Y- / Z- Direction (Depth)	Gives the vector that defines the direction of the "Depth". The direction vector of the width and the depth together define the orientation of the Building 3D Model in the room.
Width / Depth / Height	Gives the width, depth and height of the object.
Additional Info	Depending on the chosen object additional info can be set here, if applicable, e.g. door depth of the rack door.

Regarding the TERAPOD project the Importer can handle the following objects/Main Categories in the Area Category "Data Centre":

- Racks (Sub Categories: Unity, Symmetrix, VBlock, Universal, Connectrix and metal cabinet)
- Columns
- Walls/Windows
- Curtains (Sub Categories: thin and normal)

To demonstrate the above described generic import, the models of the following csv-file are imported and shown in Figure 37.

```
EAreaCategory;EMainCategory;SubCategory;ModelName;Xposition;Yposition;Zposition;XdirectionWidth;YdirectionWidth;ZdirectionWidth;XdirectionDepth;YdirectionDepth;ZdirectionDepth;Width;Depth;Height;AdditionalInfo
Datacenter;Rack;Unity;Rack1;0;0;0;1;0;0;0;1;0;0;0,6;1,5;2,5;DoorDepth:0,05
Datacenter;Rack;Unity;Rack2;2,5;0,25;1,5;0;1;0;0;0;-1;1;1,5;1,75;DoorDepth:0,05
Datacenter;Rack;Unity;Rack4;3;0;0;1;0;-0,5;0;1;0;0;0,6;1,5;2,5;DoorDepth:0,05
```





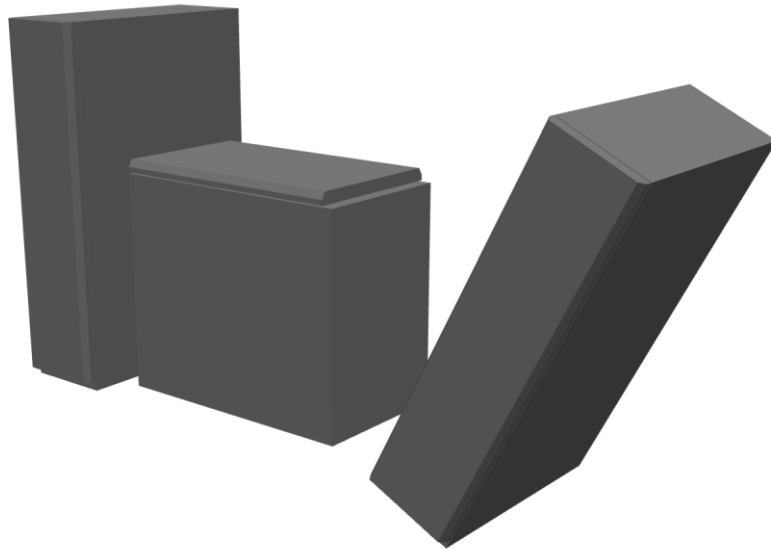


**Figure 37: Exemplary Building 3D Collection based on generic Importer**

The whole data centre results in a complex 3D model illustrated in Figure 38.

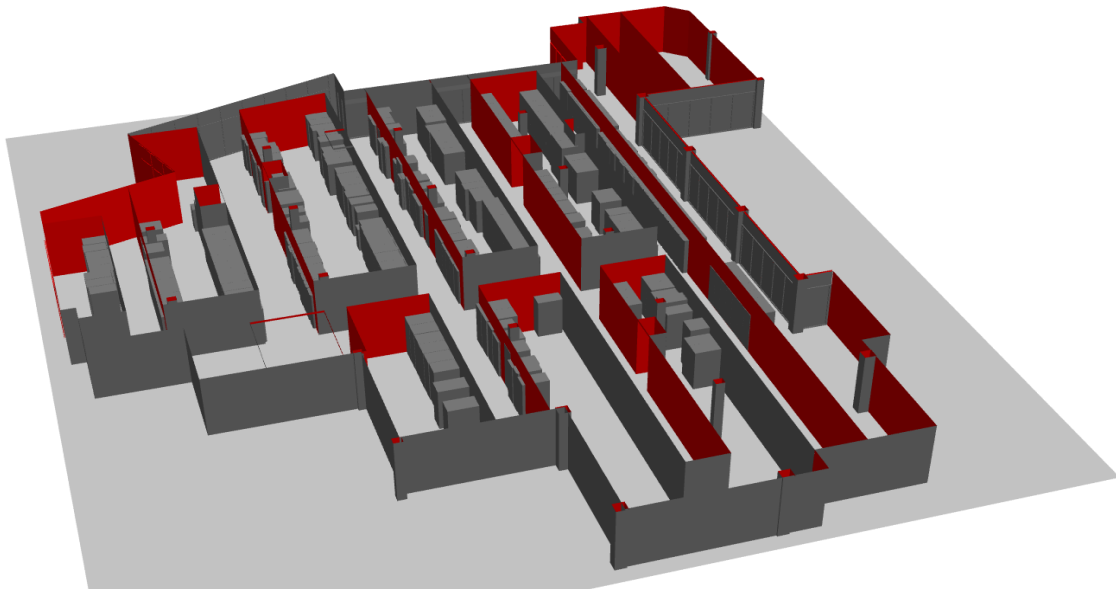


**Figure 38: 3D Model of the Dell EMC Research Data Centre**

### 3.3 Material Parameter Calibration

Using proper material parameter is a pre-requisite for obtaining realistic simulation results since propagating rays change their behaviour when they encounter material and the kind of behavioural change of rays highly depends on the material parameter. The best way to find out material parameter is measuring every single material which is used in target environment. However, measuring every single material takes time and effort. Therefore, we are do a reference measurement including material interaction and figuring the material parameter out backwards. By comparing real measurement and simulation results, it is possible to categorize interaction with material in addition to the attenuation of signal due to the interaction with encountering surfaces of obstacles. However, there are many other factors which can directly or indirectly influence the measurement results such as system stability of measuring devices, roughness of material and additional unknown and unwanted noise. Using this knowledge, material parameters for simulation can be calibrated in order to fine-tune the material parameter for achieving possibly better compatible simulation results.



Before start to explain the calibration method, explaining of transfer-matrix method [12] is helpful to understand following chapters. The transfer-matrix method is widely used model for estimating reflected and transmitted electromagnetic wave while the wave propagates through multi-layered medium having different refractive index. Which we have also used for the entire simulation in order to figure out the impact of interaction with material. In Figure 39, the general geometry of applying transfer-matrix method on single-layer is shown since the simulation environment contains only single-layered structure not multi-layered.

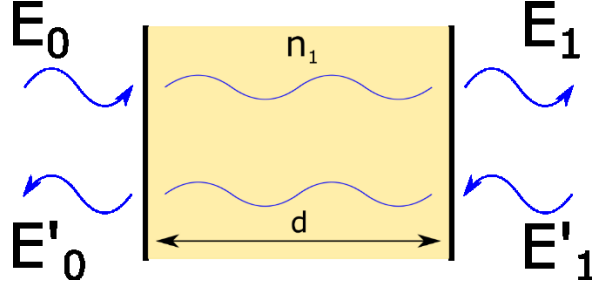


**Figure 39: Illustration of propagating electromagnetic wave through a medium having different refractive index**

In which the as mathematical matrix form of relating rays is structured like following

$$\begin{pmatrix} E_0 \\ E'_0 \end{pmatrix} = \frac{1}{t_{0,1}} \begin{pmatrix} 1 & r_{0,1} \\ r_{0,1} & 1 \end{pmatrix} \begin{pmatrix} e^{i\delta} & 0 \\ 0 & e^{-i\delta} \end{pmatrix} \frac{1}{t_{1,0}} \begin{pmatrix} 1 & r_{1,0} \\ r_{1,0} & 1 \end{pmatrix} \begin{pmatrix} E_1 \\ E'_1 \end{pmatrix} = \begin{pmatrix} m_{1,1} & m_{1,2} \\ m_{2,1} & m_{2,2} \end{pmatrix} \begin{pmatrix} E_1 \\ E'_1 \end{pmatrix} \quad (3.1)$$

Where  $t_{x,y}$  and  $r_{x,y}$  are fresnel transmission and reflection coefficients in the perspective that electromagnetic wave propagate from x to y. Here, phase shift in the medium with refractive index  $n_1$  is represented as  $\delta$  which is like following

$$\delta = \frac{2\pi}{\lambda} n_1 d \cos \theta \quad (3.2)$$

Hereby, the reflection and transmission coefficients are represented as follows:

$$r = \frac{E'_0}{E_0} = \frac{1}{m_{1,1}} \quad (3.3)$$

$$t = \frac{E_1}{E_0} = \frac{m_{2,1}}{m_{1,1}} \quad (3.4)$$

To calibrate material parameters, the simulated annealing method [13] is applied which is originally based on the simulation method of thermal annealing of heated solids. This algorithm is based on



comparing the previous state and the current state of randomly varied parameters. First, the algorithm requires an initial setting  $(T, n, c)$ . Herewith,  $T$  represent temperature,  $n$  means iterated time which starts with 0 and  $c$  means a decreasing factor of temperature. After setting the initial factors, the algorithm starts to compute differences of previous value of function  $f(x_n)$  and current value of function  $f(x_{n+1})$  with randomly changed input parameters of  $x_{n+1}$  such as the following equation:

$$\Delta f_n = f(x_{n+1}) - f(x_n) \quad (3.5)$$

where the function  $f(x_n)$  results from comparing the path loss difference of real measurement and simulated results like the equation below. Herewith, reflection loss from the material using transfer-matrix method is computed in which following four parameters are essential inputs as explained previous: incident angle, frequency, refractive index and also thickness of material

$$f(x_n) = \sqrt{\frac{\sum_1^i (Y_{i\_measured} - Y_{i\_simulated})^2}{i}} \quad (3.6)$$

where  $Y_{i\_measured}$  is the measured value of the path loss of a certain ray, while  $Y_{i\_simulated}$  is the simulated value of the path loss of the corresponding ray using the material parameter set of  $x_n$ . In every iteration  $n$ , a new set of parameters  $x_{n+1}$  is freshly generated and  $\Delta f_n$  is computed, and this is compared to the previous value of  $\Delta f_{n-1}$ . If  $\Delta f_n < 0$ , then  $f(x_n)$  for further computation is updated with the current value of  $f(x_{n+1})$  since  $f(x_{n+1})$  is more similar to the real measurement than  $f(x_n)$ , in other words, more realistic material parameter has been used for  $f(x_{n+1})$ . While, if  $\Delta f_n \geq 0$ , the assigning of the current value of  $f(x_{n+1})$  is determined with probability  $P$  following the equation for assigning a certain degree of probability to escape the local minima and to search for further global minima.

$$P = e^{-\Delta f_n * T} \quad (3.7)$$

When the iteration  $n$  is done, temperature  $T$  is reduced with the decreasing factor of  $c$ , and this iteration process is repeated until the current temperature  $T$  falls below the minimum temperature  $T_{min}$ .

### 3.3.1 Categorization of Materials in Datacentre

First of all it is required to categorize material parameters used in simulation environment. In the simulated circumstances, the materials in datacentre have been categorized in seven different types of material:

- Concrete (assumed as gypsum plaster)
- Metal (assumed perfect conductor)
- Plastic (PC)
- Curtain (old)
- Curtain (new)
- Curtain (thin)
- Ground (assumed as Metal plate)



Unfortunately, not all of the used materials in the datacentre could have been determined. Only various types of curtains have been measured by NPL in the framework of TERAPOD. Therefore, some material parameters have been assumed and referenced from [14] and [8] whose values are listed access in Table 10, whereby concrete is assumed as gypsum plaster since it is one of the well-known material to be painted on the surface of internal walls and pillars. Furthermore, plastic has been assumed as polycarbonate and the material parameter of ground is initially set as like metal. The results of the curtain measurement are given by the refractive index shown in Figure 40 and the absorption coefficient shown in Figure 41.

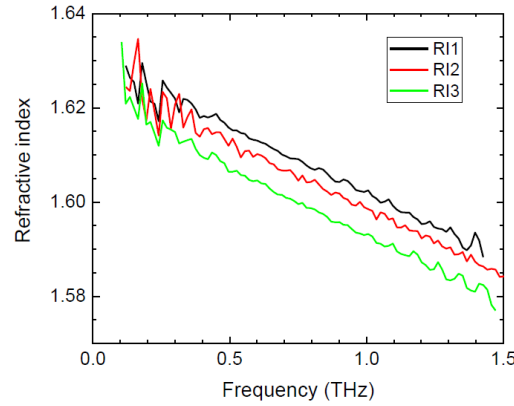


**Figure 40: Refractive index of the plastic curtains**

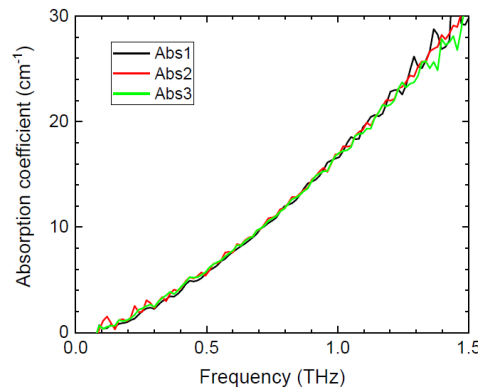


**Figure 41: Absorption coefficient of the plastic curtains**

**Table 10: Material parameters depending on material category**

Material Category	$\epsilon_r'$	$\tan \delta$	Thickness [m]
Wall (gypsum plaster) <sup>1</sup>	2.55	$5.31 \cdot 10^{-2}$	$8.2 \cdot 10^{-3}$
Plastic (polycarbonate) <sup>1</sup>	2.75	$1.61 \cdot 10^{-2}$	$3.65 \cdot 10^{-3}$
Curtain (old) <sup>2</sup>	2.63	$2.19 \cdot 10^{-2}$	$5 \cdot 10^{-3}$
Curtain (new) <sup>2</sup>	2.6	$2.39 \cdot 10^{-2}$	$5 \cdot 10^{-3}$

<sup>1</sup> This material parameters have been referenced from [14].

<sup>2</sup> This material parameters have been measured by NFL (thickness of material is uniformly assumed as 5 mm).

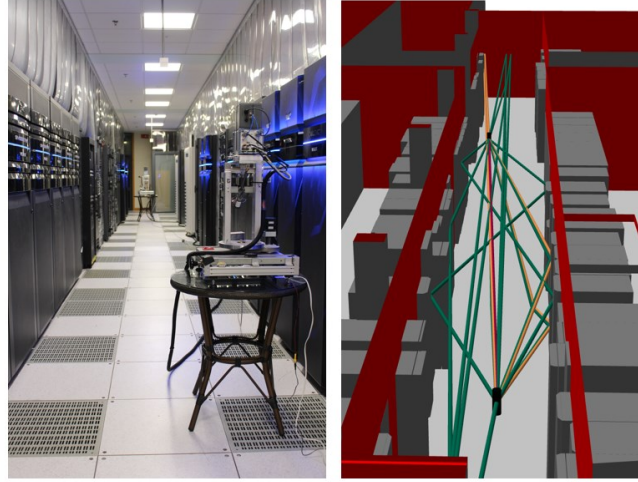


Curtain (thin) <sup>2</sup>	2.62	$2.29 * 10^{-2}$	$5 * 10^{-3}$
-----------------------------	------	------------------	---------------

Where  $\varepsilon_r'$  means real part of relative permittivity,  $\tan \delta$  stands for loss tangent (dielectric loss) which is the ratio of real part and imaginary part of relative permittivity, and thickness is the width of the interacting material. Metal was assumed to act as a perfect conductor with a reflection coefficient of 1. In the model, the racks, the ceiling and the floor are assumed to be made out of metal.

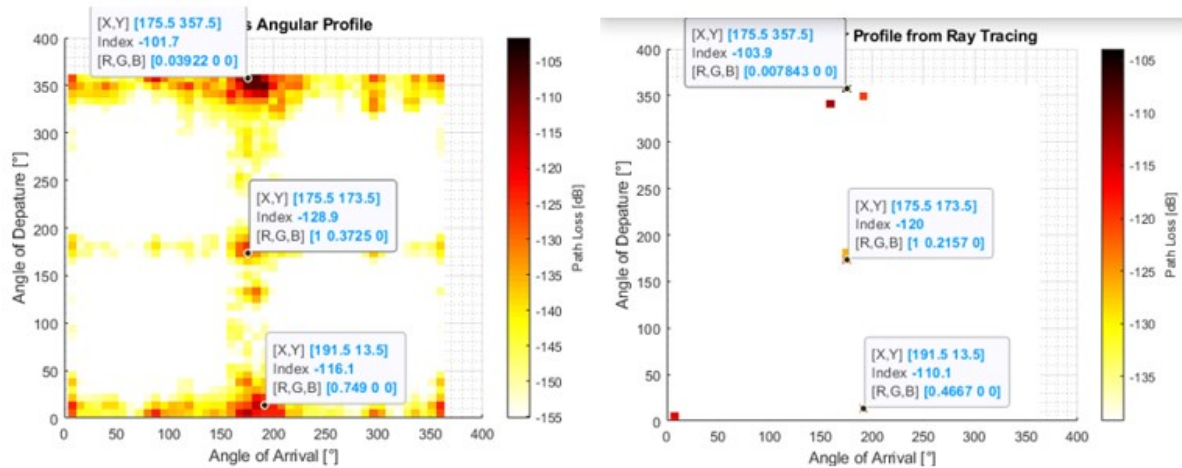
### 3.3.2 Comparison of Measurement and Simulation

First the PAP from the FO measurements will be compared with the simulation. Therefore, all setups were rebuild in SiMoNe. Here we will representatively discuss GC FO lcv and ToR FO sa.



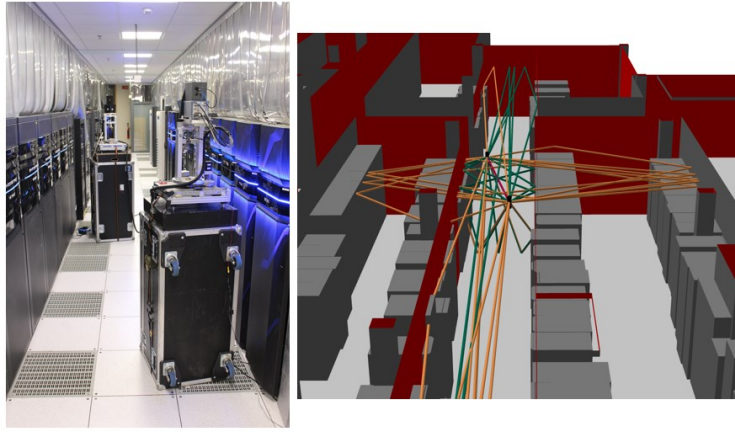
**Figure 42: setup of GC FO lcv in the DC (left) and in SiMoNe (right)**

Figure 42 shows the setup and the ray tracing in SiMoNe for GC FO lcv. The direct path is marked in red. Reflected rays are drawn in green and transmitted rays in orange. First, one can see that the majority of the rays actually lies in the horizontal plane that is scanned during the FO measurements. That confirms that this measurement methodology is effective in comparison to the whole azimuth and elevation scan. Comparing the ray tracing with the measurement in Figure 43 one can see that the most important paths are captured by the ray tracing. The accuracy of the angles and the delay is in the order of several degrees and 1 ns, respectively.



**Figure 43: Comparison of the GC measurement and ray tracing simulation**





**Figure 44: setup and ray tracing of ToR FO sa**

Also the ToR FO sa simulations of the setups shown in Figure 44 confirm the good accuracy in terms of angle and delay. In **Fehler! Verweisquelle konnte nicht gefunden werden.** the most important MPCs of the ToR FO sa simulation are marked. All important MPCs are captured by the simulation and the good match in terms of delay and angle means that the propagation and interactions points are well determined via ray-tracing.

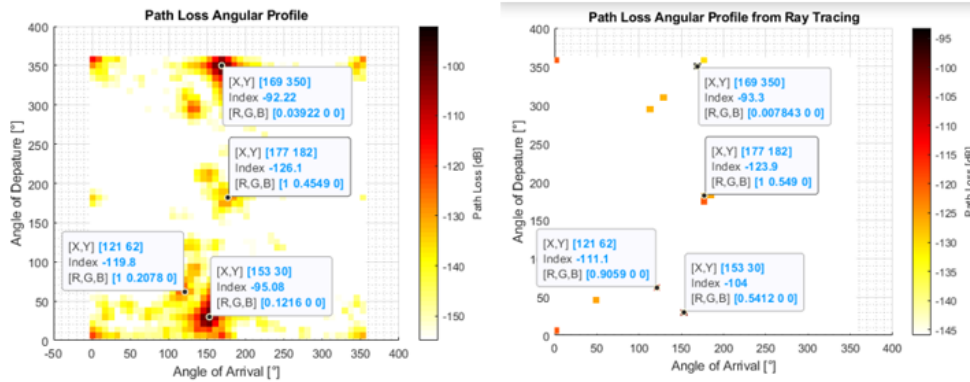


**Figure 45: Comparison of the ToR measurement and ray tracing simulation**

One notable fact is that the accuracy of the amplitude is not really persuading. This fact will be discussed in the following parts.

Since the material parameters are not completely one to one compatible with authentic material parameters used in datacentre, it is beneficial to compare the impact of interaction with material and propagating ray in the sense of reflection loss. What should be first done before comparing reflection loss of material is to check the accuracy and reliability of measurement result by comparing the free space attenuation of simulation result with that of measurement, since simulation results are computed using a mathematical model containing propagation distance and frequency and not considering any other factors, e.g., measurement environment or system stability, which raises unpredictable additional attenuation. The six different free space loss (LOS) paths of simulated and measured value are compared and shown in Table 11. Where it indicates that the difference of free space loss, i.e., margin of additional attenuation, lies between 0.91 and 3.89 dB or in another perspective 0.07 and 1.06 dB/m.

**Table 11: Comparison of six different free space path loss**

Path ID	1	2	3	4	5	6
Measured value [dB]	101.7	89.36	91.37	103	92.22	100
Simulated value [dB]	103.94	93.25	93.25	103.91	93.3	102.51





Gap of values [dB]	2.24	3.89	1.88	0.91	1.08	2.51
Gab of values [dB/m]	0.17	1.06	0.51	0.07	0.29	0.23

In Table 12 **Fehler! Verweisquelle konnte nicht gefunden werden.**, reflection attenuation due to the interaction of material is compared using the measured value and the simulated value with transfer-matrix method. In which entirely 14 paths have been compared and these are categorized in six different types of material. Here the measured value of reflection attenuation is not directly measured but post computed by subtracting mathematical free space loss from the measured value of the entire attenuation of each path. For computing material interactions can take into account various mathematical models. Of these, the transfer-matrix method model has been used for the simulation.

**Table 12: Comparison of measured value and simulated value of reflection attenuation at materials**

Material Category & ID <sup>3</sup>		Measured value in [dB] <sup>4</sup>	Simulated value in [dB] <sup>5</sup>
Concrete (gypsum plaster)	1	11.78	12.72
	2	3.94	12.72
	3	2.74	12.72
	4	14.93	12.71
Metal	1	22.35	0
	2	13.85	0
	3	3.65	0
	4	20.81	0
Plastic (polycarbonate)	1	2.85	2.93
Curtain (old)	1	28.26	10.24
	2	25.04	13.44
Curtain (new)	1	0.9	9.8
Curtain (thin)	1	33.58	13.11
	2	34.77	14.13

As notable in Table 12, the measured values and simulated values sometimes have a mismatch of up to 22 dB. While some of the simulation results, e.g., two of concrete and plastic cases, have a deviation lower than 3 dB, the majority of the first order reflections are not simulated to a satisfactory extend.

To explain this considerable discrepancy of reflection attenuation, first, it is vital to mention that a mismatch of simulation value and measurement comes from simulation design error. In other words, building information of the scenario consists of a two dimensional plane without any other further

<sup>3</sup> Path ID identifies the number of compared paths within material, i.e., four results have been compared in concrete (gypsum plaster) case while one result in plastic (polycarbonate)

<sup>4</sup> This value is posteriorly resulted by subtracting the free space loss using mathematical equation  $FSPL = (\frac{4\pi d}{\lambda})^2$  from the measured value, see Figure 42 to Figure 45.

<sup>5</sup> This value has been resulted by using transfer-matrix method considering material parameters given in Table 10.



detailed design features of the plane, i.e., any shapes such as holes, scratches and roughness on the surfaces are not realized in our simulation environments. Actually, this points can make difference of simulation results and actual measurement since rays are partly scattered, refracted and reflected with various angles unlikely to be reflected as only specular angle of surfaces when rays account for those non-uniform shapes. This results in naturally increased value of predicted reflection loss of the material in the real field, i.e., weaknesses in the received signal. This is one of the potential explanations for differences between simulation value and measurement of metal. The reflection coefficient of metal is assumed to be one, in other words, total reflection happens when propagating electromagnetic wave is incident on metal surfaces. Reference measurements at a metal plate have shown that the reflection loss of this metal plate is lower than 3 dB. Another reason for greater loss is that the rack bodies are made out of coated metal. This introduces another attenuation of at least 3 dB which was measured in an extra setup. In our simulation environment, most of materials made of metal are found at the devices, e.g., database server in datacentre and the casing of devices is modelled as a smooth plane. However, in the real case, the outer planes of devices are not completely flat but consist of many holes, splits, curvatures and special forms which cause reduced reflection and speckle so that receiver receives relatively reduced signal compared with only specular reflection case. Therefore, in the case of high reflection loss, rays actually encounter special forms, e.g., ports, and reflect from those points of devices, not off flat uniform planes.

Second point of explanation of difference is premised on the simulation uncertainty. Hereby, simulation uncertainty does not mean only brevity of simulation set up of environment described above but includes also shortage of simulator's capacity. A principle of the simulator is based on ray-tracing. Which can trace only interaction points on the material considering the specular angle. However, rays in the real field show a certain beam divergence from the point of departure. Additionally, not only specular reflection occurs but also diffuse and spread reflection off the surfaces. With respect to this point, it is possible to explain why reflection loss of gypsum plaster indicates a big difference even when they are reflected from the same material. During measurement, a writing desk was standing beside the wall where the ray-tracer has detected a ray reflected from that wall. For brevity of simulation environment, the desk has been overlooked. However, regardless of the implementation of the desk, phenomena of huge difference to the simulation result and measurement are unlikely to be detected since the ray-tracer considers only interaction points, not the entire behaviour of the whole incident spot having a diameter of 2 m on the desk.



**Figure 46: Writing desk at the end of the aisle**





Finally, in the case of curtains, it could be explained with the help of Figure 47 and Table 11 where there is a big difference of simulation results using transfer matrix method and measurement executed by TUBS. In Figure 47 the impact of thickness on the reflection loss using transfer matrix method is shown on the basis of existing rays.

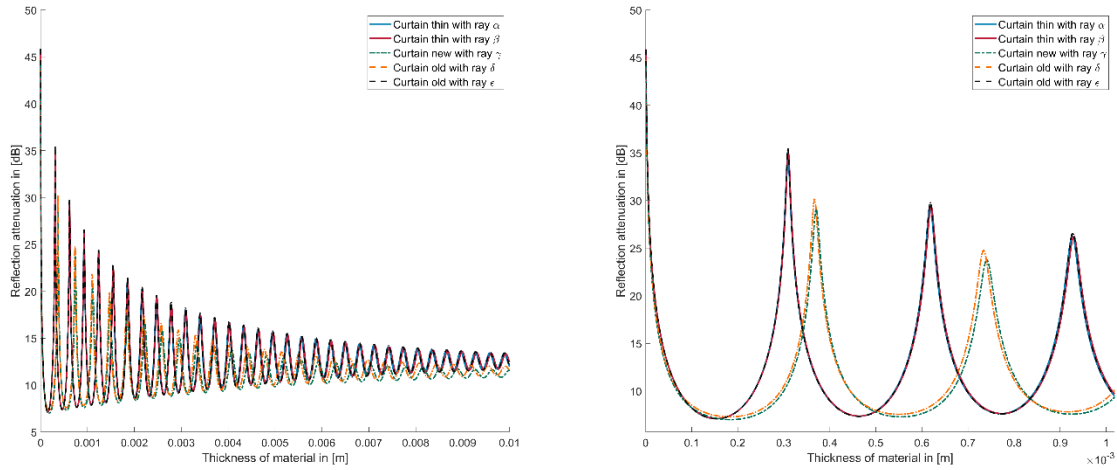


**Figure 47: Variation of reflection attenuation with different thickness of interaction material using transfer-matrix model**

Figure 47 shows obviously the Fabry-Perot etalon effect in which optical waves are bounded inside of two parallel surfaces. The transparency of the material depends on the free spectral range in other words the length of the cavity influences the reflected or transmitted intensity. The corresponding mathematical equation is given by

$$i\lambda = 2nL \cos \theta \quad (3.8)$$

where  $i \in \mathbb{N}$ ,  $\lambda$  represents wave length,  $n$  represents refractive index,  $L$  represents length of cavity and  $\theta$  represents angle of the light which travels inside of the cavity.

Discussing in further detail, the reflection loss of each ray is computed applying knowledge of angle of incidence and measured data of material parameter to transfer matrix method while the thickness of material changes from 1  $\mu\text{m}$  to 1 cm with 1  $\mu\text{m}$  step. In fact that graphs of reflection loss of ray  $\alpha$  (curtain thin), ray  $\beta$  (curtain thin) and ray  $\epsilon$  (curtain old) possess almost identical trend while ray  $\gamma$  (curtain new) and ray  $\delta$  (curtain old) also show similar trends especially at a lower value of thickness of material under 1 cm. Actually these trends are based on the incidence angle since each group have a similar value of incidence angle around  $7^\circ$  and  $62^\circ$ , respectively. The point, which is possible to interpret from Figure 47, is the reflection loss of 6 mm thickness shows a local minimum value of fluctuation in all five cases. Another point to note is that reflection loss fluctuates sensitively depending on change of thickness such that its value fluctuates de facto from around 7 to 45 dB under the applied condition. The measurement values of five cases lie in this variation range. If additional unwanted system loss shown in Table 11 is regarded, the range of possible thickness to fulfil the explanation of difference between simulation value and measurement will be further enlarged. As an example, the ray  $\gamma$  (curtain new) encounters the material with the incident angle of  $62.63^\circ$ . A part of ray  $\gamma$  is transmitted through the encountering material and right away changes its propagation properties, e.g., direction, phase and velocity. Which occurs due to variation of refractive index between two medium in this case air and curtain shown in



Table 13 . Therefore, the part of transmitted ray  $\gamma$  propagates inside of the curtain with the incidence angle of  $33.36^\circ$ .

**Table 13: refractive coefficient and resulted angle between air and curtain (new)**

Material	Complex refractive coefficient n	Angle [degree]
Air	1.0003	62.63
Curtain ( new )	1.615 - 0.02i	33.36

**Table 14: reflection and transmission coefficient between air and curtain**

coefficient	TE	TM
$r_{0,1}$	$-0.49 + 0.0065i$	$-0.059 - 0.0034i$
$t_{0,1}$	$0.51 + 0.0065i$	$0.058 + 0.0049i$
$r_{1,0}$	$0.49 - 0.0065i$	$0.059 + 0.0034i$
$t_{1,0}$	$1.49 - 0.0065i$	$1.71 - 0.015i$

Particularly, using our transfer-matrix model, the second peak of reflection loss lies on 0.37 mm thickness of material. Where reflection and transmission coefficients used for equation 3.1 are shown in Table 14 and the coefficients are separately described in each case for TM and TE. Applying this value into equation 3.1, it is possible to figure out that the reflection coefficient of TM ( $r_{tm}$ ) and TE ( $r_{te}$ ) are achieved using equation 3.3 and amount totally to 7.02% while the second bottom of reflection loss lies on 0.555 mm and results 86.38% of reflection coefficient. This variation comes from change of  $\delta$  which is linear proportional to material thickness of d.

In order to understand the impact of each variable of transfer-matrix model on the reflection attenuation, the result of reflection attenuation is computed using changes of input variables. This gives an overview and general knowledge about the impact of variation of pertaining material parameters on the reflection attenuation using transfer-matrix model. In particular three parameters: angle of incidence, thickness and the real part of relative permittivity have been highlighted since this is essential values for running transfer-matrix method, and two of these have been varied within a given range in each case. In every case, the resulting reflection loss with specific parameters is depicted with various colours. First of all, the correlation of real part of relative permittivity and thickness of material with reflection attenuation is presented in Figure 48. Where the real part of relative permittivity is varying from 0.1 to 10 with 0.1



increment while the thickness of material changes from 10  $\mu\text{m}$  to 1 cm with 10  $\mu\text{m}$  step. Herewith, the angle of incidence is fixed at  $45^\circ$  and  $\tan \delta$  is assumed as zero.

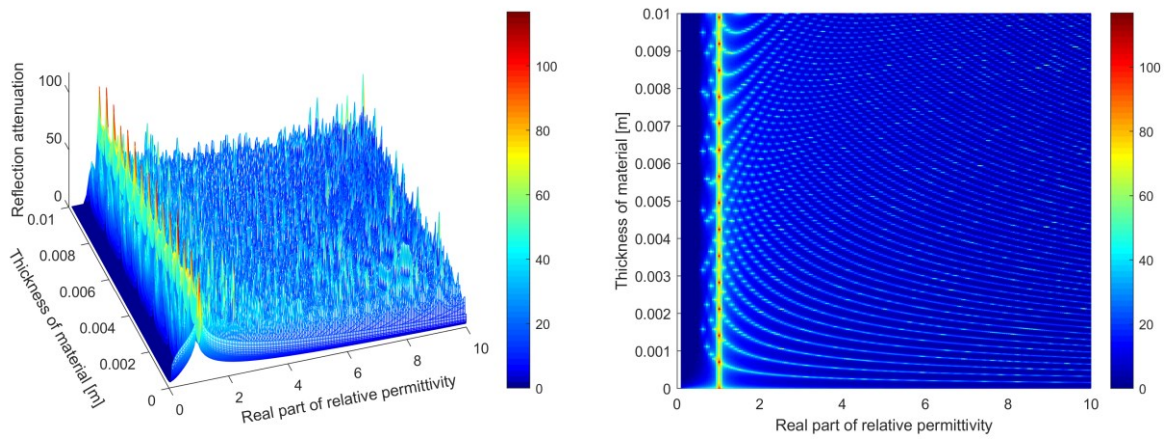


**Figure 48: 3D (left) and 2D (right) depiction of reflection loss against thickness and real part of relative permittivity using transfer-matrix method**

In Figure 49, the relationship of reflection loss with angle of incidence and real part of relative permittivity  $\epsilon_r'$  is investigated under the provided conditions. Whereby, the angle of incidence varies from zero to  $90^\circ$  increasing by  $0.1^\circ$  and the value of the real part of relative permittivity  $\epsilon_r'$  is changed in the range of 0.1 to 10 with 0.1 increment while the thickness of material  $d$  is assumed to be 1 mm and its value is maintained constant. Here also,  $\tan \delta$  is set as zero.

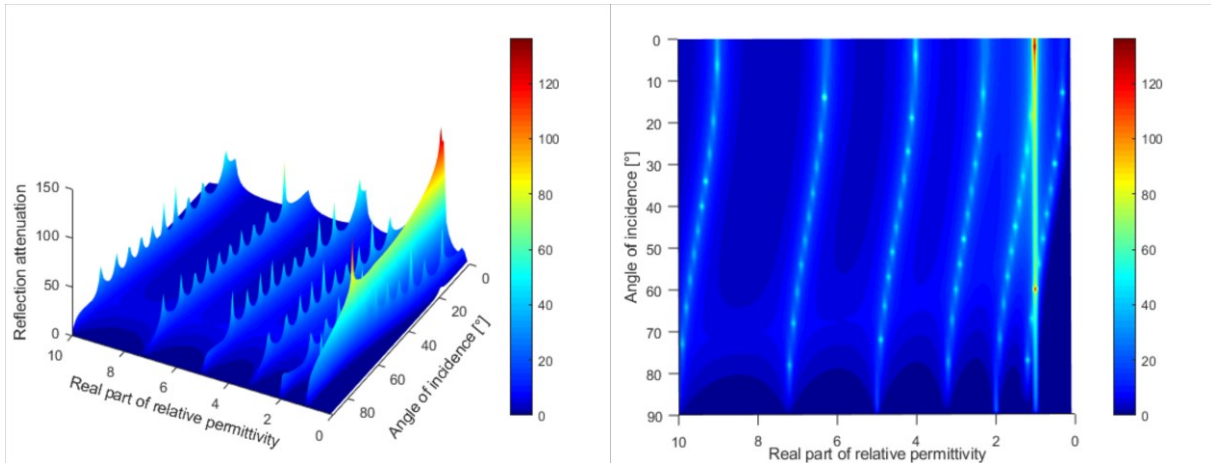


**Figure 49: 3D (left) and 2D (right) depiction of reflection loss against angle of incidence and real part of relative permittivity using transfer-matrix method**

The correlation between reflection loss with angle of incidence and thickness of interaction material is depicted in Figure 50. Where the angle of incidence changes from zero to  $90^\circ$  and the thickness of material varies from 10  $\mu\text{m}$  to 1 cm. In this case, the real part of relative permittivity remains constant at the value of 2.63, which is the mean value of material parameters in Table 10 except for metal and ground. The value of  $\tan \delta$  is assumed to be zero.



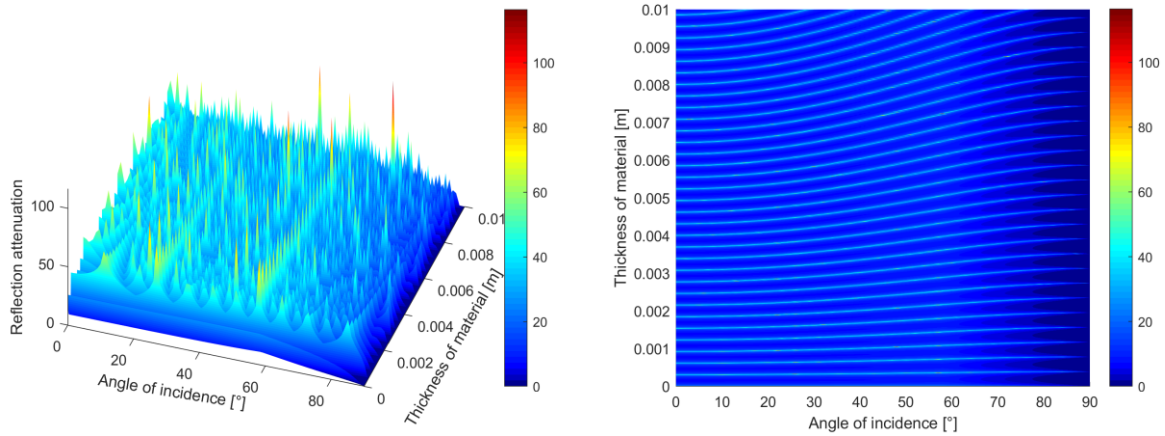


**Figure 50: 3D (left) and 2D (right) depiction of reflection loss against angle of incidence and thickness of interaction material using transfer-matrix method**

In these three figures, it is possible to recognize that the resulted reflection attenuation using transfer-matrix method fluctuates strongly based on change of one of the parameters. Besides, the relationship between reflection attenuation and three parameters seems to possess a certain pattern caused by Fabry-Perot etalon effect. Furthermore, on the condition of restriction of changeable parameter as only one, i.e., impact on reflection attenuation is limited to only one parameter such as thickness, angle of incidence and real part of relative permittivity, then reflection loss has a tendency that the value fluctuates and wobbles with some rough propensity.

### 3.4 Stochastic Channel Modelling

Currently, simulation method is widely used and became a mainstream of every single engineering field due to its convenience, safety of failure-prevention and price-competitiveness of total expenditure. The simulation method can be distinguished mainly into two types by the way of approaches. Stochastic modelling is an inductive method which gives us an overview of the characteristics of simulation of real field environment, so that first, we can get preferentially general knowledge of circumstances beforehand. Second, obtained information can be used as a foundation and planning guidelines which enable us to avoid foreseeable drawbacks and problems in advance, and further let us find out a better solution.

Stochastic channel modelling is literally to do a massive number of random variable based simulations in order to obtain meaningful data of target environment. As described previously, our target environment is one of the datacentre depicted in detail in chapter 3.2. For stochastic channel modelling, the antenna position is assumed to be 10 cm above the centre of each rack. TX and RX positions are designated in two different types shown in a simplified form in [Fig 2].



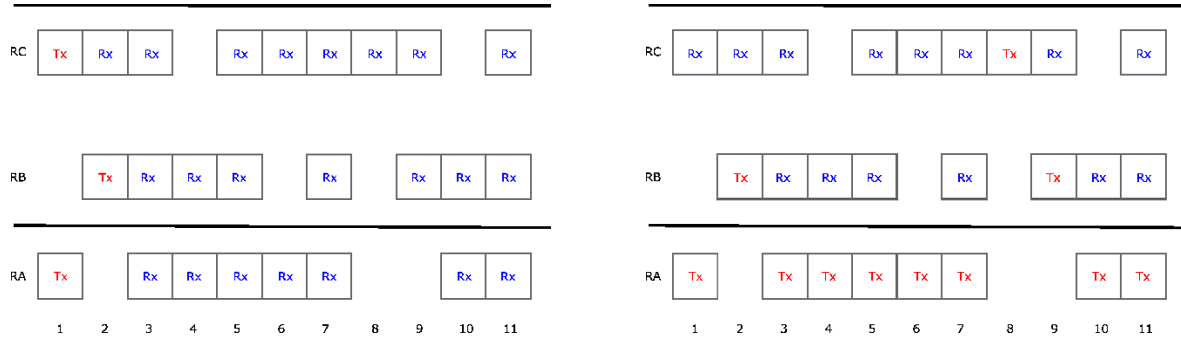


**Figure 51: Exemplary TX-RX position limiting interaction region within Chamber (Left); through Chamber (right)**

Where the racks are exemplary displayed as grey boxes which compose arrays of racks named RA, RB and RC. Above each rack, antennas are positioned and set as TX (red) and RX (blue). The arrays of racks are partly isolated with curtains represented as black lines between the arrays of racks. Which means, RA is physically and spatially separated from RB and RC while RB and RC pairs share the same physical space. We view this physical separation of racks as a chamber. In the case of a limited interaction region of rays within the chamber (hot aisle in Figure 1), the existing rays are detected only spatially isolated within surrounding curtains, see black line in Figure 51. This means, the array of racks RA is considered as a physically separated environment, while RB and RC are considered as part of the same simulation environment. In contrast, in case of considering rays not spatially separated by curtains, rays are detected and predicted including a possible TX-RX pair through the curtains (through the cold aisle in Figure 1), i.e., TX from RA and Rx from RC can make a TX-RX pair.

### 3.4.1 Propagation path types

Figure 52 shows feasible propagation paths within our simulation condition. There are in total four types of propagation paths: direct, 1<sup>st</sup> reflected, 2<sup>nd</sup> reflected and transmitted path. When the interaction region is limited as shown in Figure 51 (left), every type of propagation path is available to be detected. Direct rays (type1) are found when a TX-RX pair is under LOS condition. Reflection (type 2 and 3) can be seen when rays are reflected from curtains or racks. Additionally, transmission (type 4) can happen when a TX-RX pair fulfils the NLOS condition due to an obstacle such as racks since the height of a rack is not uniform. In the case of Figure 51 (right), reflection is not considered. Therefore a direct path (type 1) and a transmitted path through curtains or racks (type 2) are foreseeable. The consequence of path types on the simulation result is presented in Table 15.



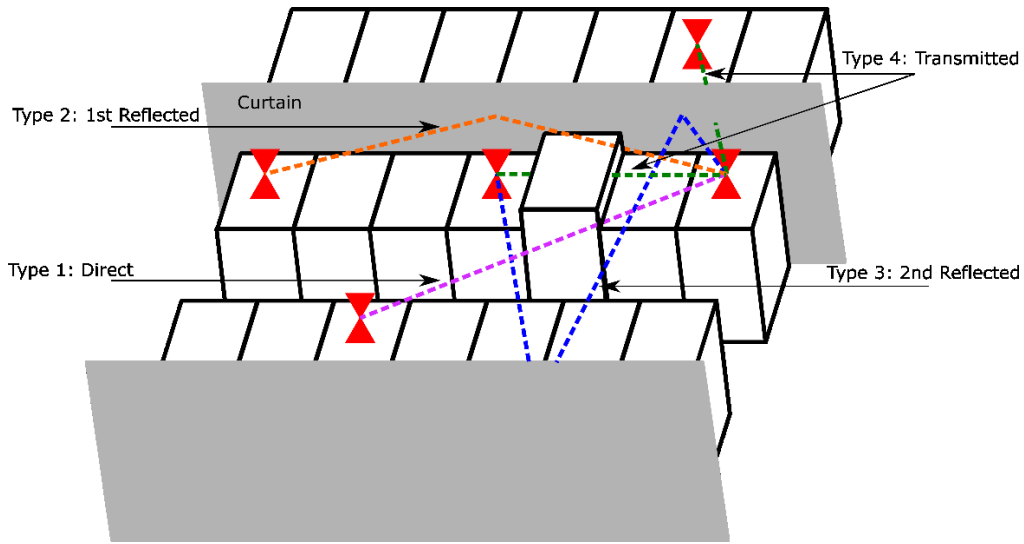


Figure 52: Propagation path types

Table 15: Number of existing rays depending on path types

	Type 1	Type 2	Type 3	Type 4
Number of path	635	1180	2665	7643

### 3.4.2 Statistical Delay Distribution

The statistical delay distributions of each propagation type are shown in Figure 53. Their delay distribution is distinguished by its propagation type accordingly: direct, reflected and transmitted. Detailed values of parameters of each distribution and type are presented in Table 16.

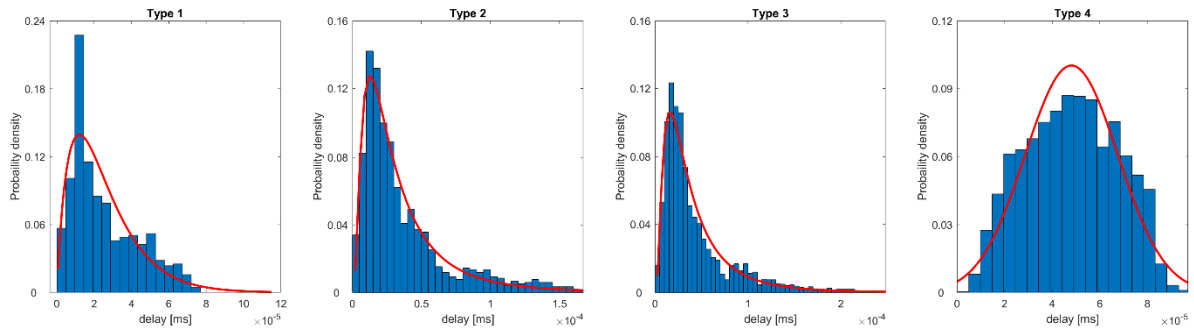


Figure 53: Delay distributions of each type of propagation paths

Table 16: Values of parameters and type of delay distribution in terms path types

Path type	Distribution type	Parameters
Type 1	Gamma	$\alpha= 1.91$ ; $\beta=1.32 \times 10^{-5}$
Type 2	Lognormal	$\mu= -10.54$ ; $\sigma=0.85$
Type 3	Lognormal	$\mu= -10.36$ ; $\sigma=0.83$
Type 4	Normal	$\mu= 4.81 \times 10^{-5}$ ; $\sigma=1.95 \times 10^{-5}$

Here delay distribution in Figure 53 is strongly related to the position of antenna respectively TX and RX. The results of type 1 to type 3 show gamma and lognormal shape whose delay distributions rise up rapidly and after the peak return back slowly. For computing ray tracing of type 1 to type 3, RXs are





placed only first index of each chassis of rackmounts array, see Figure 51 (left). Herewith, the simulation environments are spatially limited inside of so called hot aisle in Figure 1 which is surrounded by curtains. The probability of possible path between TX and RX pair is naturally high at certain distance since the TX and RX pair is available not only within same named line of rackmounts, e.g., only RB see Figure 51, but also over the line of racks within same hot aisle, e.g., between RB and RC see Figure 51. In which two different lines of rackmounts within hot aisle is not adhere closely but positioned rather with some distance. On the contrary, type 4 shows normal distribution shape since the transmission is not bounded by any objects. Additionally, RXs are weighted positioned like shown in Figure 51. Therefore, the probability of distance of TX-RX pair is distributed Gaussian shape.

Similar stochastic channel modelling has been done in the framework of IEEE P802.15 Working Group for Wireless Personal Area Networks (WPANs) [15]. In which channel modelling has been done using weigh more simplified scenario of data centre network. Within the scenario, many server chassis (rackmounts) are sited inside of the simple square shape of virtual date centre. Comparing this with our scenario, both of scenarios contain many server chassis (rackmounts) and ray tracing method has been used for finding existing rays between TX and RX. However, both scenarios are not one-to-one identical since the data centre model in [15] is designed as a simplified typical wireless data centre therefore rackmounts are evenly positioned and also the height of rackmounts is unified. But our model has been designed in order to reflect possibly similar the specific features of one of data centre. Therefore, most of important structural features have been reflected in our model, e.g., polygon shape of data centre. Comparing result with this stochastic channel modelling result in Channel Modelling Documents [15], the result shows dissimilar behaviour since the type of rays are differently defined and TX and RX positions have been divergently assigned. Nonetheless, In case of type 4 (transmission) in our model and LOS case of type 1/2, TX 1 in [15], both delay distributions show comparable behaviour since the both simulation conditions have been relatively similarly set. In case of type 1/2, TX in [15], TXs are positioned in the room corner and in our case, mostly edge of data centre. In this case both delay distribution represent Gaussian distribution shape.

### 3.4.3 Delay-Path loss Correlation

It is not surprising that delay and path loss have positive correlation since delay is directly proportional to the path length and the path loss is also positively associated with the path length. The correlation of delay and path loss is illustrated in Figure 54.

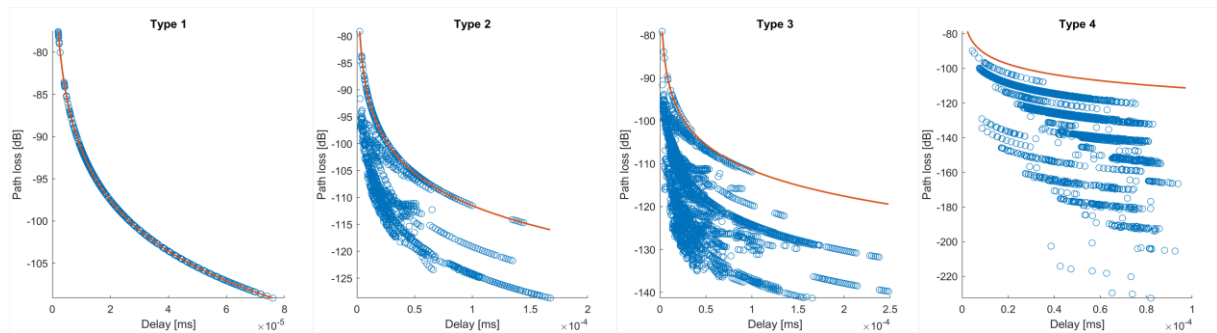


**Figure 54: Delay-Path loss correlation distribution**

where red line represents a mathematical equation of free-space loss and delay while blue points show simulation results of delay and path loss of each path. As it is possible to see in case of type 1, simulation results are sited exactly on the mathematically calculated line since type 1 is direct rays and therefore no interaction with material is happened. However, this trend is not valid any more in type 2,3 and 4 because additional attenuation comes from interaction with different materials. Nonetheless, some simulation results of type 2 and 3 are positioned on the red line. This is due to the fact that the reflection



factor of metal in the simulation is assumed to be one, as it is in the case of propagating ray interacts with any materials. Which means, the blue points sited on the red line represent the rays which were reflected from only the metal part of the simulation environment.

### 3.4.4 Angle of Departure (AoD) and Angle of Arrival (AoA)

Using 300 GHz as a carrier frequency for wireless communication has many challenges to overcome. One of the well-known challenge is the high free-space attenuation which stems from high attenuation coefficient of propagating ray. Therefore, high gain antenna is one of the general way to compensate this high propagation loss of sub millimetre-wave communication in order to achieve the required received power for successful wireless communication, i.e., enough received power for accomplishing to transform received signal into originally transmitted signal after decoding phase. Exactly on this point, the antenna pointing is at the same time a more crucial factor for successful wireless communication since the higher the gain of the antenna, the narrower its main lobe. This means that propagating rays are spatially more filtered at both the sender and the receiver pair. Therefore, in this sense, the departing and arriving direction of rays in terms of Angle of Departure (AoD) and Angle of Arrival (AoA) provide meaningful information to better understand the general characteristics of propagating environment in this case, specifically datacentre. This is shown in Figure 55, Figure 56, Figure 57 and Figure 58 depending on the type of rays. In these figures, the probability densities of departing and arriving rays are separately shown in different colours according to the angle of elevation and azimuth. Elevation angle is represented from -90 degree to +90 degree. In which -90 degree stands for positive z-axis, 0 degree for x-y plane and +90 degree for negative z-axis. The azimuth angle varies from -180 degree to +180 degree, where 0 degree refers to positive y-axis, from 0 degree to -180 degree means anti-clockwise angles from positive y-axis to negative y-axis while from 0 degree to +180 degree represents clockwise angles from positive y-axis to negative y-axis.

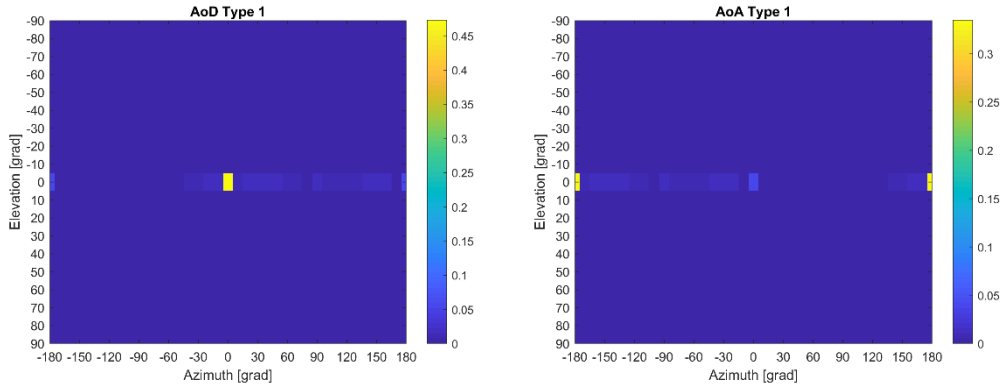


Figure 55: Probability of Angle of Departure (left) and Angle of Arrival (right) of type 1: direct

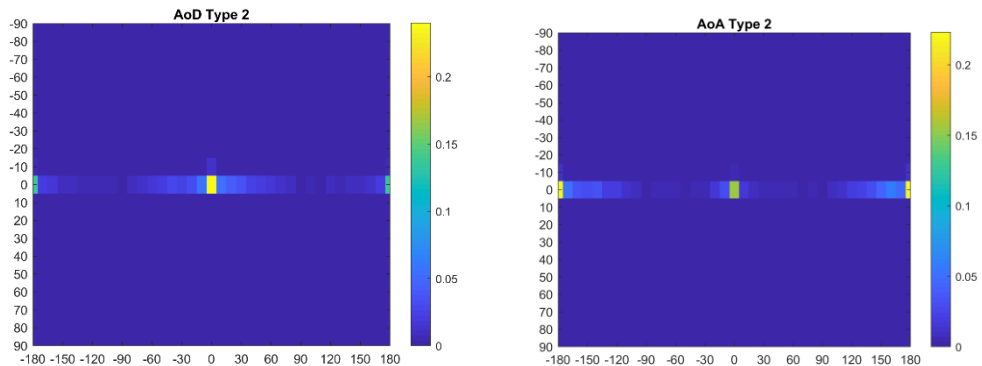
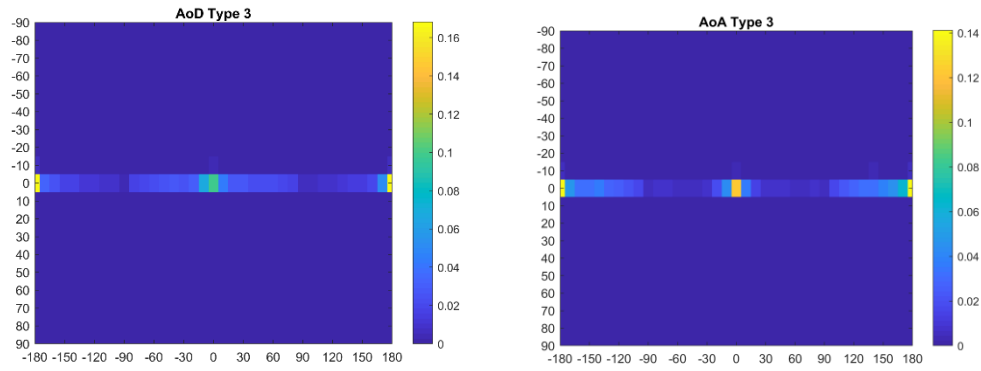


Figure 56: Probability of Angle of Departure (left) and Angle of Arrival (right) of type 2: 1<sup>st</sup> reflected







**Figure 57: Probability of Angle of Departure (left) and Angle of Arrival (right) of type 3: 2<sup>nd</sup> reflected**

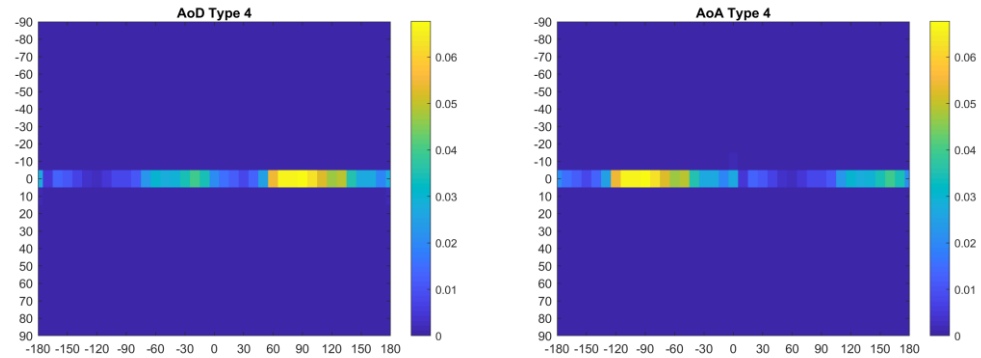


**Figure 58: Probability of Angle of Departure (left) and Angle of Arrival (right) of type 4: transmitted**

### 3.4.5 Angle-Path loss Correlation

As is shown above in chapter 3.4.4, the elevation angles of Angle of Departure (AoD) and Angle of Arrival (AoA) are more or less flat since the heights of racks are approximately comparable. Therefore, the elevation angle is insignificant due to its negligible effect on the AoA and AoD. Consequently, it implies the possibility of revealing a correlation between path loss and Angle of Departure (AoD) and Angle of Arrival (AoA). In Figure 59, Figure 60, Figure 61 and Figure 62, probability density of correlation of propagation loss, angle of arrival and angle of departure is shown specified by the category of ray type and coloured by its probability density.

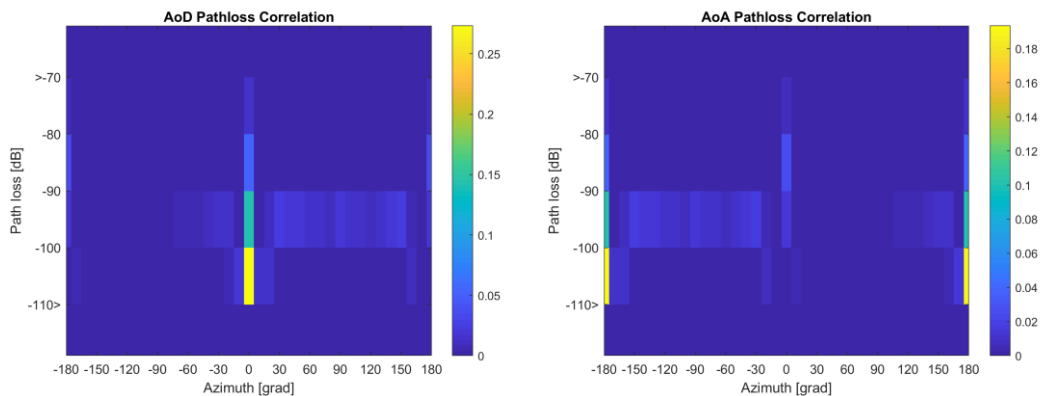


**Figure 59: Probability of Angle Path loss Correlation of type 1: direct**



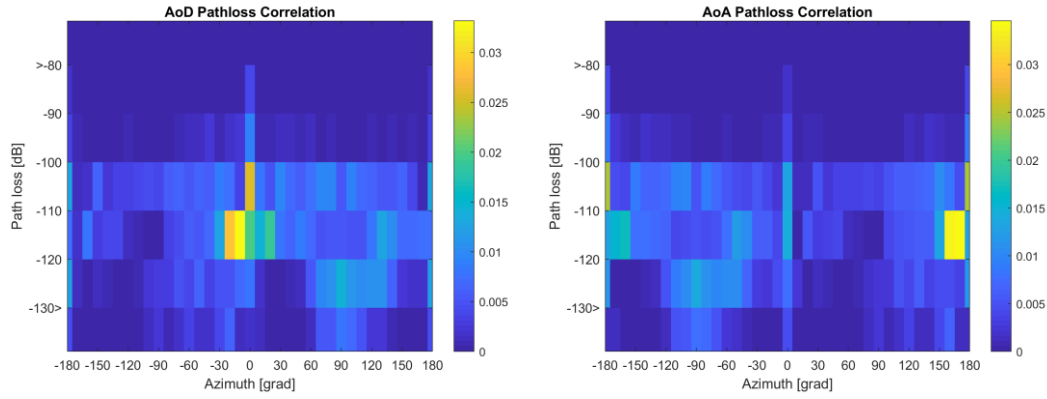


**Figure 60: Probability of Angle Path loss Correlation of type 2: 1<sup>st</sup> reflected**

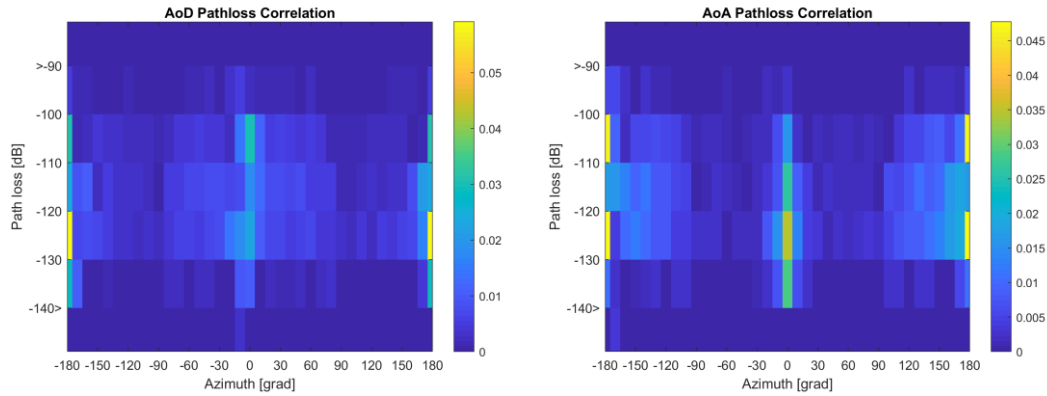


**Figure 61: Probability of Angle Path loss Correlation of type 3: 2<sup>nd</sup> reflected**

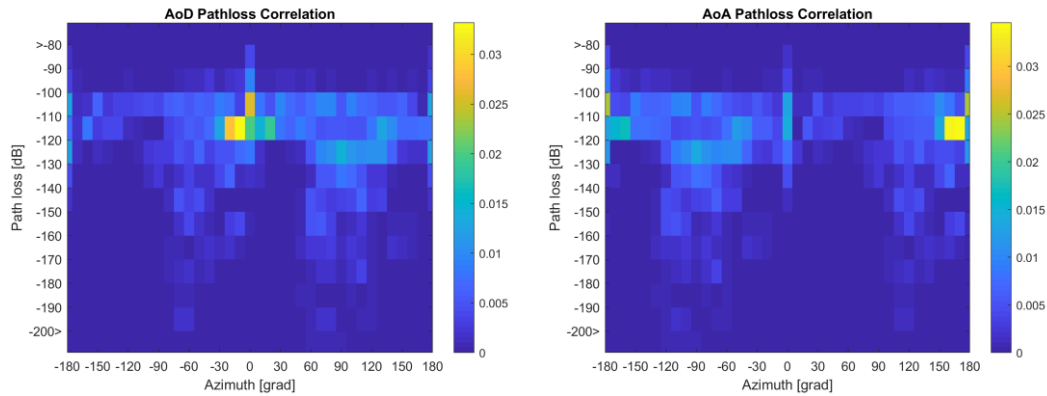


**Figure 62: Probability of Angle Path loss Correlation of type 4: transmitted**



## 4 Transmission Measurements in the Environmental Chamber

Transmission measurements were performed in an environmental chamber under a range of temperature and humidity conditions. The purpose of these measurements was to verify that under expected conditions of Terapod use case scenarios loss variation will be negligible.

The use case conditions were defined in D2.1 & D2.2 as:

- Temperature range: 18-27 °C
- Humidity range: 20%-80% RH (relative humidity)

The test conditions for transmission measurements in the environmental chamber encompassed and significantly exceeded the ranges of use cases. They were as follows:

- Temperature range: 10-40 °C
- Humidity range: 20%-90% RH (relative humidity)

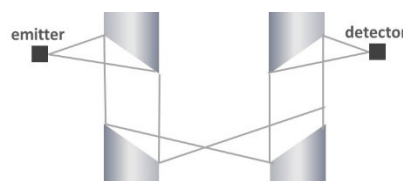
A commercial environmental chamber was employed (SANYO Gallenkamp PLC), shown in Figure 63. The internal size of the chamber was 2 x 2 x 2.2 m.



**Figure 63: Photograph of the environmental chamber employed in transmission measurements**

Transmission was measured using a frequency-domain spectroscopy (FDS) system (Toptica Photonics TeraScan 1550). A THz FDS employs two lasers with offset wavelengths; dedicated semiconductor-based antennas – commonly referred to as “photomixers” – convert the beat signal into a THz wave. Varying the wavelength offset between the two lasers tunes the THz frequency. FDS is a continuous-wave, coherent measurement system. The Toptica TeraScan system uses PIN diodes as emitter and detector, and has a tuning range of 30-2100 GHz with a resolution of 30 MHz. It was used in these experiments due to its ability to provide accurate transmission measurements at low frequencies below 100 GHz and due to its high frequency resolution.

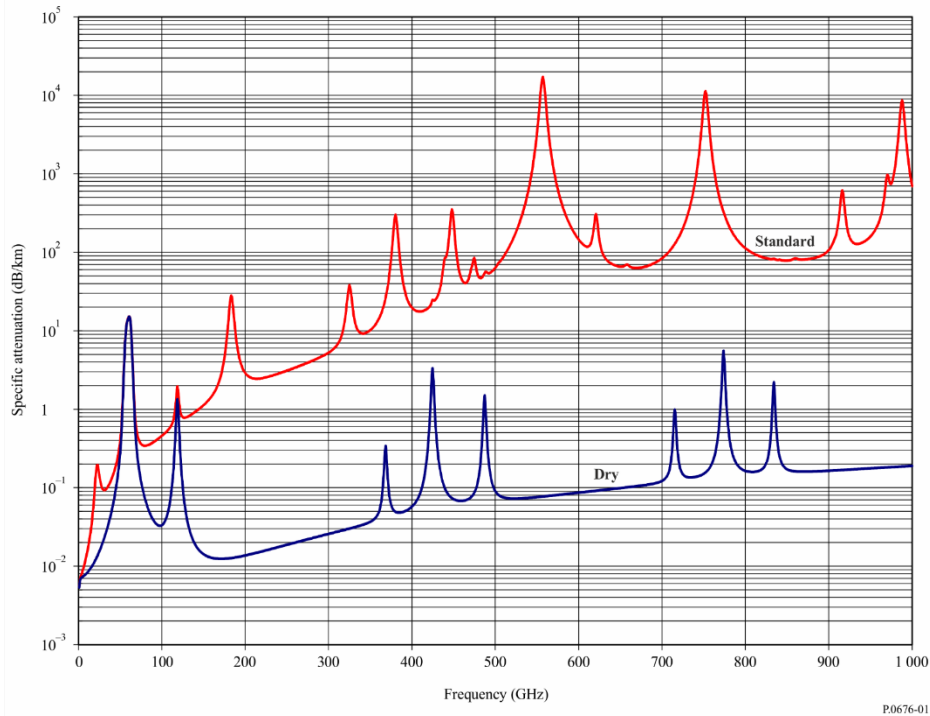
The measurement configuration is shown in Figure 64. Four parabolic mirrors were used to guide the THz beam from the emitter to the detector with minimal loss due to beam divergence; the beam path length was 0.8 m.



**Figure 64: Schematic diagram of the THz beam path in the transmission measurement setup**

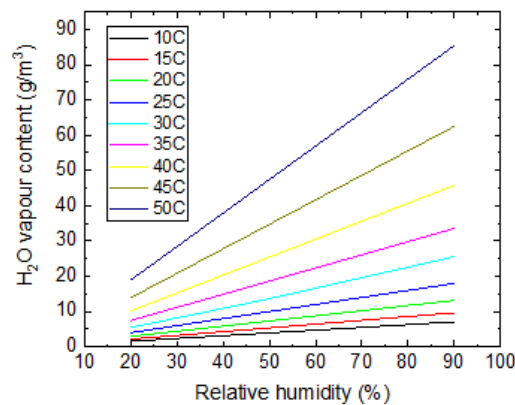


Transmission attenuation due to absorption by atmospheric component gases has been studied in detail and widely reported in the literature. Particularly relevant to THz communications is the report ITU-R P.676-12 “Attenuation by atmospheric gases and related effects” (08/2019) from the International Telecommunications Union. Figure 65 shows transmission attenuation at frequencies up to 1000 GHz for dry and standard atmospheric conditions.



**Figure 65: Atmospheric attenuation due to absorption by gases. Dry: 2.2 g/m<sup>3</sup> H<sub>2</sub>O; standard: 7.5 g/m<sup>3</sup> H<sub>2</sub>O. From ITU-R P.676-12.**

In the frequency range pertinent to THz communications, atmospheric absorption is caused predominantly by two gases: oxygen and water vapour. Of these, only the water vapour content varies with environmental conditions. The content of water vapour in the atmosphere, measured as g/m<sup>3</sup>, is determined by the combined factors of temperature and relative humidity (RH). Figure 66 shows the dependence of water vapour density on relative humidity and temperature. Referring to Figure 66 and the measurement conditions listed above, it is seen that the water vapour density range was between 3-46 g/m<sup>3</sup>.



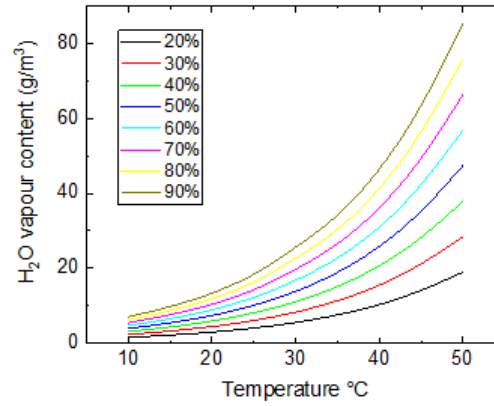


**Figure 66: Dependence of water vapour content on ambient relative humidity and temperature**

Figure 67 shows the expected attenuation at selected frequencies (100, 220, 300 GHz) for a range of water vapour densities similar to the experimental conditions. These frequencies were selected as lying in the transmission windows and being target frequencies for Terapod devices.

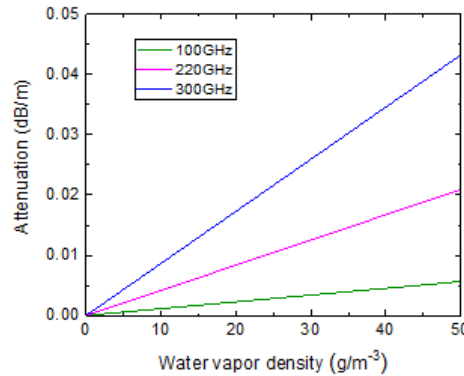


**Figure 67: Expected atmospheric attenuation at 100, 220 and 300 GHz as a function of H<sub>2</sub>O density**

For example, attenuation at 300 GHz and 50 g/m<sup>3</sup> H<sub>2</sub>O would be 0.043 dB/m. This is an order of magnitude below the minimum loss detectable using the experimental setup described above, which was 0.5 dB. Therefore no detectable variation in the transmission signal was expected at these frequencies within the range of the experimental conditions. This is confirmed by Figure 68 which shows the detected signal at 100, 220 and 300 GHz as a function of water vapour density. It is seen that the signal remains constant within the measurement error, confirming negligible attenuation in the Terapod use case scenarios.



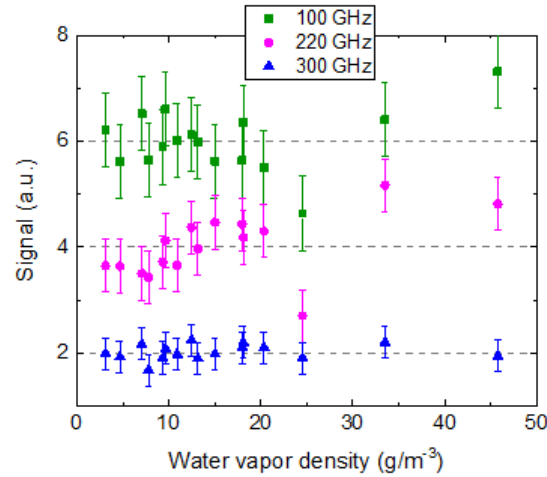


**Figure 68: Transmission signal at 100, 220 and 300 GHz as a function of water vapour density, showing absence of detectable dependence.**

The transmission measurement approach was validated by examining attenuation at the frequency of the water vapour absorption line at 557 GHz, depicted in Figure 7.

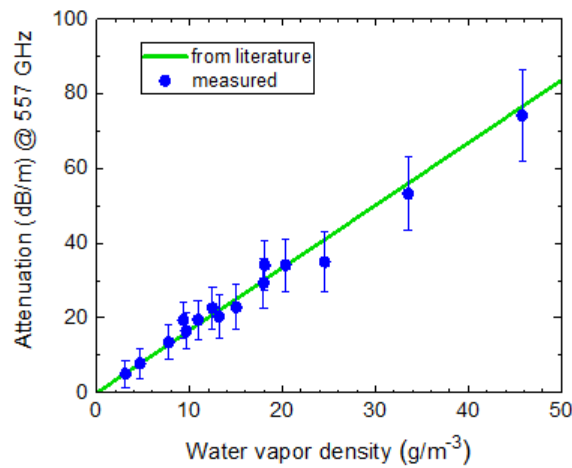


**Figure 69: Attenuation by water vapour at 557 GHz, showing agreement with literature.**

Summary: Environmental chamber measurements of signal transmission were carried out in the range of ambient conditions relevant to Terapod use-case scenarios. The measurements confirmed negligible attenuation by atmospheric absorption under those conditions.



## 5 Conclusion/Further work

This deliverable presents the main results of task T4.2 of work package 4 of the TERAPOD project. First, the measurement campaign and the methodology are explained. The corresponding analysis shows the different aspects of the spatial and temporal characteristics of the THz channel in a data centre environment. The delay spread and the angular spread are calculated to further characterise the properties of the radio channel in the different application scenarios.

With regard to the ray tracing simulations it is shown that meaningful results can be produced by this simulation method. Therefore, ray tracing is a promising tool for further simulation and modelling approaches for sub-THz and THz communication systems.

Stochastic modelling was performed based on various ray tracing simulations showing the angle distributions and the correlation of the delay and path loss.

Finally, the measurements in collaboration of NPL and TUBS in the environmental chamber show that the impact of water vapour absorption in the data centre environment has a negligible effect.



## References

- [1] J. M. Eckhardt et al. D4.3 Initial characterisation of systems, TERAPOD deliverable, 2019
- [2] Niamh O'Mahony et al. D2.1 Initial Requirements and Scenario Specifications, TERAPOD deliverable 2018
- [3] Niamh O'Mahony et al. D2.2 Revised Requirements and Scenario Specifications, TERAPOD deliverable 2019
- [4] J. M. Eckhardt, T. Doeker, S. Rey, T. Kürner, "Measurements in a Real Data Centre at 300 GHz and Recent Results", *Proc. European Conference on Antennas and Propagation*, Krakow(Poland), April 2019
- [5] S. Rey, J. M. Eckhardt, B. Peng, K. Guan, and T. Kürner, "Channel sounding techniques for applications in THz communications: A first correlation based channel sounder for ultra-wideband dynamic channel measurements at 300 GHz," in *Proceedings of the 9th International Congress on Ultra Modern Telecommunications and Control Systems and Workshops (ICUMT)*, Nov 2017, pp. 449–453.
- [6] Zhen Xiao-dan *et al.*, „The Implementation of Wiener Filtering Deconvolution Algorithm Based on the Pseudo-Random Sequence“. In: *American Journal of Circuits, Systems and Signal Processing*, Vol. 2, No. 1 (Nov. 2016), pp. 1–5.
- [7] Robert Kessel. „Wiener Filter Estimation of Transfer Functions“. In: *Journal of the Experimental Analysis of Behavior*, Vol. 81, No. 3 (Mai 2004), pp. 289–296.
- [8] K. Guan *et al.*, "Channel Characterization for Intra-Wagon Communication at 60 and 300 GHz Bands," in *IEEE Transactions on Vehicular Technology*, vol. 68, no. 6, pp. 5193-5207, June 2019.
- [9] D. M. Rose, J. Baumgarten, S. Hahn, and T. Kürner, "Simone – simulator for mobile networks: system-level simulations in the context of realistic scenarios," in *2015 IEEE 81st Vehicular Technology Conference (VTC Spring)*, pp. 1–7, May 2015.
- [10] N. Dreyer and T. Kürner, "An Analytical Raytracer for Efficient D2D Path Loss Predictions," *2019 13th European Conference on Antennas and Propagation (EuCAP)*, Krakow, Poland, 2019, pp. 1–5.
- [11] Andreas F. Molisch. *Wireless Communications (2nd. ed.)*. Wiley Publishing, 2011.
- [12] Sánchez-Soto, Luis L.; Monzón, Juan J.; Barriuso, Alberto G.; Cariñena, José F. The transfer matrix: A geometrical perspective *Physics Reports*, Volume 513, Issue 4, p. 191-227.
- [13] S. Rao, *Engineering Optimization: Theory and Practice*, New Jersey: Wiley, fourth edition, 2009
- [14] R. Piesiewicz, "Propagation Aspects and Performance Study of Future Indoor Wireless Communication Systems at THz Frequencies", Dissertation, Herzogenrath: Shaker Verlag, 2009
- [15] A. Fricke, "TG3d Channel Modelling Document (CMD)", IEEE P802.15 Working Group for Wireless Personal Area Networks (WPANs), March 2016.

